Volcanic island multi-stage construction inferred from a simple geometrical approach: Example of Réunion Island

Eric Gayer, Laurent Michon, Nicolas Villeneuve

volcanic island multi-stage construction inferred from a simple geometrical approach: Example of Réunion Island

Eric Gayer [a,*], Laurent Michon [a,b], Nicolas Villeneuve [a,b]

[a] Université de Paris, Institut de Physique du Globe de Paris, CNRS, F-75005 Paris, France
[b] Université de La Réunion, Laboratoire Géosciences Réunion, F-97744 Saint-Denis, France

* E-mail address: egayer@ipgp.fr (E. Gayer).

A B S T R A C T

The reconstruction of volcanic landforms is an effective way to assess the construction history and growth rates of volcanic structures and is a useful tool to estimate erosion rates. We propose a simple geometrical approach to reveal the location of the long term eruption centers and the general shape of eroded volcanoes within the alti tudinal range of the input data. This DEM based approach consists of finding the radial topographic profile of an eroded volcanic landform from its remaining surfaces, by coupling two independent and simple mathematical methods (linear regression and Spearman rank correlation). Here we demonstrate that this simple approach is suitable for circular to elliptical (up to an ellipticity of 0.5) and to some extent for asymmetrical volcanoes, and we apply it to Réunion Island. Our results confirm previous conclusions from geological observations and data re quiring more complex instrumentation. We confirm that the center of long term volcanic activity of Piton des Neiges remained stable for the past 1.4 Myr while Piton de la Fournaise has been migrating eastward for ~300 kyr. Our approach also reveals that Piton des Neiges is the dominant volcano in Réunion and that Piton de la Fournaise is a smaller edifice built on its edge. Moreover, despite the contribution of two other volcanoes in the construction of Réunion, we suggest that the Piton des Neiges has rapidly become the main structure of the whole island and has subsumed the previous volcanic centers . Finally, we use our approach to model the magmatic activity of Piton des Neiges, and suggest a deceleration of its magma emission rate since 2Myrs.

1. Introduction

Volcanic landforms, and more specifically volcanic islands, have long been used as natural laboratories to study erosion processes (and controls) because their evolution reflects the competition between construction and degradation (Karátson et al., 2012; Ferrier et al., 2013a, 2013b; Murphy et al., 2016; Gayer et al., 2019). The destruction of volcanoes can originate from volcano tectonic processes, or struc tural instabilities (Thouret, 1999). Additionally, climate, through precip itations, continuously triggers the erosion of volcanoes (e.g. river incision, landslides; Ferrier et al., 2013a) which often threatens human populations (e.g. landslides, large floods; Terry et al., 2002; Garcin et al., 2005; Allemand et al., 2014). Together, these factors stimulate study of volcanic erosion, and quantitative geomorphological studies are considered as an effective method to understand volcanic landforms evolution and the extent of the associated societal concerns.

The geomorphic analysis of a volcanic terrain is facilitated by the re markable symmetry and regularity of many volcanoes (Francis and Abbot, 1973; Lacey et al., 1981; Karátson et al., 2010) and by the fact that erosion initiated by river incision often leaves parts of a volcano preserved, even after much of the original surface has been eroded (e.g. Ollier, 1988). Using the geometry and ages of uneroded remnants and digital elevation models (DEM), volcano characteristics and pre erosion surfaces can be reconstructed (Hildenbrand et al., 2008; Karátson et al., 2010; Lahitte et al., 2012; Salvany et al., 2012; Ferrier et al., 2013a; Favalli et al., 2014; Gayer et al., 2019) to constrain the mor phology of the volcano at different stages of growth (e.g. Salvany et al., 2012; Gayer et al., 2019; Dibacto et al., 2020). By subtracting the current topography from a pre erosion modeled surfaces, it is possible to calcu late the volume of material eroded over a given period of time and esti mate the erosion rates and the erosion history of a volcanic landform (e.g. Ferrier et al., 2013a; Gayer et al., 2019).

The same principle, but using pre and post eruption topographies and characteristics, has been used to estimate growth rates, magma fluxes, magma volumes, and the dynamics of magmatic processes, as well as to establish the history of volcano construction (Lahitte et al., 2012; Dibacto et al., 2020). In addition, volcano characteristics, such as the radial profiles or locations of the long term eruptive centers have been used to study volcanic processes including eruption style, gravita tional spreading, vent migration and growth trends (Francis and Abbot, 1973; Székely and Karátson, 2004; Karátson et al., 2010; Grosse et al.,

2012; Lahitte et al., 2012; Dibacto et al., 2020). Combining geological, geophysical and geochemical data with such characteristics makes it possible to model the evolution of single volcanoes but also of volcanic islands to better understand the evolution of eruptive complexes (Hildenbrand et al., 2004; Lahitte et al., 2012).

Except for volcanoes where magma emission is primarily located along radial rift zones, building elongated or strongly asymmetric edifices (e.g. Dieterich, 1988; Carracedo, 1994), many studies have characterized the regular shape of volcanoes (Francis and Abbot, 1973; Lacey et al., 1981; Grosse et al., 2009, 2012, 2014; Karátson et al., 2010). For example, studies have described volcanoes profiles using a near constant slope on the lower flank and a profile that is concave upwards near the summits, or using a logarithmic curve on the lower half and either a straight line or a parabolic arc to define the upper half of volcanic edifices (Lacey et al., 1981; Karátson et al., 2010). The temporal evolution of the volcano shape has also been addressed, since as the volcano grows, its shape progressively departs from a conical profile with constant slope to a logarithmic profile (e.g. Francis and Abbot, 1973). While volcanoes can have various profiles, depending on their type (e.g. shield volcanoes or stratovolcanoes; Lahitte et al., 2012; Grosse and Kervyn, 2018) and their age (Grosse et al., 2009), a large fraction have a near circular symmetry. This facilitates the elucidation of pre erosion or pre eruptive original morphology and allows the estimation of erosion and construction histories and rates (e.g. Salvany et al., 2012; Karátson et al., 2016; Gayer et al., 2019; Dibacto et al., 2020).

Several methods exist to reconstruct the geometric characteristics (center and radial profile) and the original shape of a volcanic edifice from the remnants of a volcanic landform. On the one hand, when an important fraction of the edifice remains, the fitting of parametric surfaces is usually preferred (Lahitte et al., 2012; Salvany et al., 2012). On the other hand, a more geometric and general approach can be used to estimate the radial topographic profile (defined by the remaining surfaces) and the geometric surface of revolution (e.g. Rowland, 1996; Lahitte et al., 2012; Favalli et al., 2014; Gayer et al., 2014). Yet, reconstruction of volcanic relief characteristics or modeling of the original surfaces can be challenging, especially when the edifice morphology departs from circularity, and may require more or less sophisticated mathematical methods (e.g. kriging interpolation or n degree polynomial fit) and specialized software (e.g. Geographical Information System).

Here we present a simple and easy to implement geometric approach to reveal long term eruption centers (as centers of mass) and average flank shapes of eroded volcanoes within the altitudinal range of the input data. By providing these parameters, our method can be used as a first step toward original volcanic landform reconstruction. First, we present the utility and robustness of our method by applying it to ten volcanoes with a wide range of types and geometries. Some of these have been used in previous studies on reconstruction methods so we can compare our approach to past results (Karátson et al., 2010; Favalli et al., 2014). Second, we apply our method to the volcanoes on Réunion Island, and use it to explore the evolution of an eruptive complex. Our analysis of Réunion includes submarine and subaerial domains and we interpret our results in the context of the evolution of the whole island.

2. Method

The techniques of reconstruction of volcanic landforms typically requires a complex analysis of the spatial organization of data points taken from un or slightly eroded topographic surfaces in order to constrain the original shape of a given volcano (e. g. Karátson et al., 2010; Lahitte et al., 2012). In this study, we present a simple methodology that reveals both the center of the long term volcanic activity, and the original volcano shape (over the elevation range of the remaining surfaces), which can then be leveraged in more complex analyses. Our technique is related to the conventional approach that consists in finding the best 2D arrangement of the remaining surfaces of a volcanic edifice (e.g. Rowland, 1996; Lahitte et al., 2012; Favalli et al., 2014; Gayer et al., 2014). However, it couples two independent and simple mathematical methods in a way that is very easily implemented in any programming language or even within a spreadsheet (a Python version is available on GitHub https://github.com/egayer/ConeCone).

2.1. Concept

The surface morphology of a volcano is largely controlled by exogenous processes resulting from the accumulation of the eruptive products (e.g. Naumann and Geist, 2000). The original shapes of volcanoes depends on various factors such as slope stability, the hydraulic resistance of the flow of magma (Lacey et al., 1981), the magma type (e.g. viscosity), the effusion rate, the type and distribution of vents and the tectonic control (e.g. rift zone activity). However, because of such construction by accumulation, any point located at high altitude on a volcano is closer to the eruptive center than points located at lower elevation (disregarding the summit crater). Consequently, all elevation profiles around the center of a volcano show a negative correlation between distance and elevation, and the combination of all the radial profiles of an edifice defines its general shape (Fig. 1).

In a Distance to Center vs. Elevation (DCE) diagram (Fig. 1b), every point of a quasi circular and near symmetrical volcano is narrowly distributed along a curve or a line (since several mathematical expressions exist to define the geometric shape of different types of volcanoes; Francis and Abbot, 1973; Karátson et al., 2010, 2012; Fig. 1b). This distribution reflects the strong relationship between the location of the center of the edifice and that of any point on the volcano (elevation and distance from the center). In contrast, any irregular or asymmetrical volcanoes (e.g. affected by rift zone activity; Fig. 1c) generates a scattered distribution on a DCE diagram while retaining the negative correlation between elevation and distance of all the radial profiles (Fig. 1d).

Within this framework, the location and elevation of the remains of an ancient or dismantled volcano can be computed in a DCE diagram in order to find (i) their best arrangement and (ii) provide both the center of eruption (or of long term volcanic activity) and the general shape of the original volcanic morphology (within the altitude range covered by the remnants).

In the approach presented here, we propose to measure and compare the arrangement of the remnants in the DCE diagram, for all potential center locations. In other words, this approach is based on the search of the location of the center that gives the best negative correlation in the DCE diagram. As a result, the general shape of the volcanic morphology is directly given by the shape of the corresponding distribution.

One simple way to measure the strength of a relationship between two variables is to use the linear regression method. Yet, volcanic slopes are not always well represented by linear function. To account for this, we also use, in parallel, the Spearman's rank order correlation technique since it measures the strength of the association between variables on an ordinal scale (elevation and distance here), without assuming a linear relationship. Although this method avoids the problem of linearity, it is subject to other considerations, notably the potential irregularity of the flank profile. For these reasons, the methodology presented here combines the two simple and independent mathematical techniques of linear regression and Spearman correlation, in order to estimate the best arrangement (negative correlation of the radial profiles), then used to estimate the center and general shape of the volcano.

2.2. Methodology

For a given DEM of a volcanic landform, with a set of uneroded remnants (the surface points of which are called control points hereafter), each grid point of the DEM can be viewed as a potential long term eruptive center. For each of these potential centers, the distance with respect

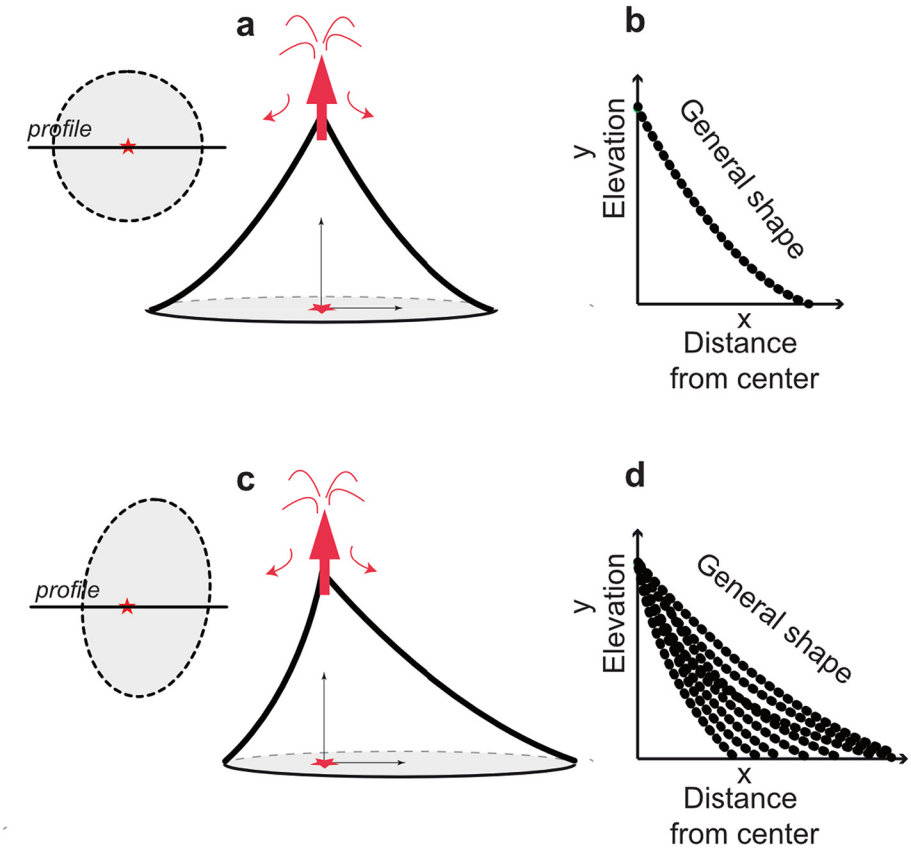

Fig. 1. First-order geometry of volcanoes in a Distance-to-Center vs. Elevation (DCE) diagram. (a) Footprint and 3D representation of a theoretical regular volcano presenting a conical shape with changing slope. The red star represents the location of the center of eruptions. (b) 2D representation of the same volcano in a DCE diagram, defined as a Cartesian coordinate system with the eruptive center as origin, the radius of the conical volcano as the x-axis, and the axis of the cone as the y-axis. For a regular conical volcano, all points of its surface fall on a curve (or line in the case of a constant slope cone) showing an anti-correlation between radius and elevation and describing the average profile of the edifice. (c) Footprint and 3D representation of a theoretical non-regular volcano. (d) In the DCE diagram, the asymmetry of the edifice yields a scattered distribution of all the points of the surface of the volcano, that still describes the anti-correlation between radius and elevation.

to the control points can be calculated and plotted against elevation to measure their distribution (Fig. 1b, d).

For linear regression, the center of the edifice is given by the grid point for which the distribution of the control points in the DCE dia gram, provides the best fitting straight line through the control points (i.e. the best coefficient of determination of the fitted regression line). Consequently, the general profile of the volcano is represented by the distribution of the control points in the DCE diagram.

To guard against non linearity we also perform a second estimate of the best arrangement of the control points using the Spearman rank co efficient of correlation (*rho*, e.g. Well and Myers, 2002). For each grid point of the DEM of the volcanic landform under investigation, *rho* is calculated as follows:

$$rho \quad \frac{cov(Rk, zk)}{\sigma Rk\, \sigma zk} \tag{1}$$

where *Rk* is the distance between the control points and the grid point, and *zk* is the elevation of each uneroded remnant, both converted to ranks. As the Spearman's correlation coefficient measures the strength of monotonic relationships, the center of the edifice is given by the grid point that provides the best Spearman's coefficient (the closest to −1). Here again, the corresponding arrangement of the control points in the DCE diagram provides the general shape of the volcanic edifice.

Regardless of the mathematical method used to determine the best arrangement of the control points (linear regression or Spearman's rank coefficient correlation), our approach gives, in a single step, the center of long term volcanic activity and the general radial shape of a given volcano. Although it does not provide the original 3D surface of the volcano, this could be modeled in an independent and subsequent step using the functions that best fits the general profile established with our method.

Finally, there are different ways of implementing our approach. In the one presented in this section, we calculate the linear regression and the Spearman's coefficient with each grid point of the DEM as a potential center of the volcanic edifice under investigation. This meth odology requires a GIS software or a programing language. However, another way to implement this approach is to use optimization tools, which can be found on any programing languages but also in widely used software such as MS Excel (Excel Solver), making our approach ac cessible to a very wide range of users.

2.3. Accuracy of the method

Fresh stratovolcanoes often present remarkable regular and sym metric shapes but composite volcanoes or basaltic volcanoes affected by rifting activity or faulting may be irregular and asymmetric (Grosse et al., 2009; Lahitte et al., 2012; Grosse and Kervyn, 2018). As stated in Section 2.1, the more irregular a volcanic structure is, the more scattered the radial profiles are (Fig. 1d), and the more difficult it is to estimate a general shape. Yet, this does not necessarily imply that the analysis of an irregular volcano characterized by a scattered combination of radial profiles, cannot help determining the location of the long term eruptive activity.

In order to test the method presented in this paper on a variety of volcanic shapes, we first compared our results with those previously obtained with other techniques (Karátson et al., 2010; Favalli et al., 2014) on three conical to elliptic volcanic edifices: Mayon, Licancabur,

Mt. Cameroon (Table 1). Moreover, we considered seven additional volcanoes to enlarge the range of geometry (i.e. circular, elliptic or irregular) and the range of degree of symmetry (Fuji, Karthala, Ambae, Mauna Loa, Mauna Kea, Hualalai and Kohala; Table 2). Finally, we compared our results from a truncated volcano (Mt. Somma) to those from a previous study (Favalli et al., 2014). These eleven case studies span a variety of geological contexts, volcano types, eruptive dynamics, emitted products (lava flows vs. pyroclastic flows) and dismantling levels, which helps assess the accuracy of our approach for different volcano geometries.

2.3.1. Ellipticity and symmetry of volcanoes

In order to test the performance of our approach on the different types and geometries of the volcanoes listed in Tables 1 and 2, we had to characterized their shape and their symmetry (this was not possible for the dismantled edifice of Mt. Somma). Several parameters have already been used to define the shape of a volcanic edifice, such as the circularity of its base or the evolution of the circularity with elevation (Karátson et al., 2010). In the case of an elongated volcano, the circularity can be expressed, instead, as the flattening (or ellipticity, e) of the ellipse that describes its basal shape, with $e = (a - b) / a$ and where a and b are the major and minor axes, respectively. While ellipticity can be easily estimated from the contour lines of a volcano, the degree of symmetry of an edifice is less simple to quantify since it requires characterization of the symmetry.

For each volcano, we averaged the ellipticities at different elevations. As an example, for the Mayon volcano, we calculated the ellipticities of the closed contour lines from 600 to 2200 m (every 200 m), and then computed a weighted averaged from the area delimited by each contour line. To estimate the ellipticity of each contour line, we modeled an ellipse that has the same second central moment as the region delimited by the contour line, and calculated e from the modeled major and minor axis, a and b (Fig. 2a).

This approach reveals the planes of symmetry of a given edifice. Indeed, any volcanic landform, whether slightly to strongly elongated, has two potential planes of symmetry that correspond to the major axis a or minor axis b of the ellipse that describe its geometry in the XY plane (Fig. 2). Therefore, the general axis of symmetry of a volcano (in the XY plane) can be determined from the average orientation of the major axis a of each contour line weighted by the area of that contour line (Fig. 2). This axis of symmetry allows to define a vertical plane of symmetry, and based on the comparison of the volume of the edifice on both sides of this plane, we calculate the degree of symmetry of a volcano as the percentage of similarity on both sides of the plane following:

$$\text{Degree of symmetry} \quad 100 \times \left(1 - \frac{\sum \left(\left|z_{x,y} - z_{x',y'}\right| \times s\right)}{Vt}\right) \tag{2}$$

where Vt is the total volume of the edifice, calculated from the minimum elevation of the contour line used in the calculation of the ellipticity (i.e. 600 m for Mayon), $z_{x,y}$ is the elevation of a grid point on the DEM, $z_{x',y'}$ its mirrored elevation across the axis of symmetry, and s is the area of the DEM cells.

The ellipticities and degrees of symmetry of the ten volcanoes are listed in Table 2. Ellipticities range from 0.03 to 0.50 and the degrees of symmetry range from 82 to 96%. With an ellipticity close to 0, Mayon is a quasi circular volcano, and its degree of symmetry of 96% means that the difference in volume on both sides of the plane of symmetry account for only 4% of the total volume. In contrast, Mt. Cameroon and Ambae volcanoes have a strong ellipticity of 0.5 and 0.4 and degrees of symmetry of 94 and 89%, respectively (Table 2). Out of the ten studied edifices, Kohala presents the strongest asymmetry (82%) due to the deep incision of its eastern flank (Lamb et al., 2007).

Table 1
Performance of the method using altitudinal profiles as control points.

Volcano	Grid res. (m)	Ellipticity	Degree of symmetry (%)	Profiles				Center LR		Center SP		Bootstrap on Profiles													
				N. points	r-Squared	Spearman Rho		X(m)	Y(m)	X(m)	Y(m)	N. points	Mean r-Squared	Std.Dev. r-Squared	Mean Spearman Rho	Std.Dev. Spearman Rho	Center LR					Center SP			
																	X(m)	±	Y(m)	±		X(m)	±	Y(m)	±
Mayon	91	0.03	96	354	0.929	−0.998		574,274	1,465,503	574,227	1,465,599	177	0.930	0.006	−0.9973	0.0005	574,275	116	1,465,501	112		574,242	84	1,465,599	92
Fuji	85	0.17	93	205	0.982	−0.994		293,913	3,915,754	293,937	3,915,755	103	0.983	0.002	−0.9923	0.0040	293,912	57	3,915,754	40		293,911	188	3,915,756	95
Mt. Somma	10	–	–	1098	0.922	−0.977		957,867	4,533,934	957,812	4,533,866	549	0.923	0.004	−0.9768	0.0021	957,867	41	4,533,933	70		957,810	56	4,533,860	93
Mt. Cameroon	92	0.50	94	1085	0.811	−0.909		519,522	466,025	519,419	465,889	543	0.811	0.015	−0.9091	0.0099	519,524	363	466,021	319		519,478	409	465,955	394
Licancabur	30	0.06	96	432	0.989	−0.995		614,624	7,474,487	614,633	7,474,484	216	0.989	0.001	−0.9940	0.0019	614,624	24	7,474,487	17		614,632	47	7,474,472	76

Note: Grid res. refers to DEM resolution in meter. * For Profiles: N. Points refers to the number of points of the altitudinal profile. r-squared and Spearman Rho refer to the r-squared and Spearman Rho of the LR and SP methods using all the points on profile, respectively. X(m) and Y(m) refer to the coordinates in meter (UTM) of the resulting centers using LR and SP methods. * For Bootstrap on Profiles: N. Points refers to the number of points randomly sampled over each profile for each of the 1000 runs. Mean r-squared refers to the average of the 1000 r-squared resulting from the Linear Regression method (LR). Std.Dev. r-squared refers to the standard deviation of the 1000 r-squared. Same for Mean Spearman Rho and Std.Dev. Spearman Rho from the Spearman correlation method (SP). X(m) and Y(m) refer to the average coordinates in meter (UTM) of the centers resulting from the 1000 runs using LR and SP methods. Errors are given as 3-sigma errors.

Table 2
Performance of the method using control points randomly picked from delimited regions.

Volcano	Grid res. (m)	Ellipticity	Degree of symmetry (%)	Bootstrap on delimited regions												
				N. points	Mean r-Squared	Std.Dev. r-Squared	Mean Spearman Rho	Std.Dev. Spearman Rho	Center LR				Center SP			
									X(m)	±	Y(m)	±	X(m)	±	Y(m)	±
Mayon	91	0.03	96	1000	0.875	0.005	0.9963	0.0003	574,176	69	1,465,529	67	574,171	32	1,465,701	26
Fuji	85	0.17	93	1000	0.883	0.005	0.9573	0.0037	294,177	99	3,915,810	105	294,259	167	3,916,044	141
Mt. Somma	10	-	-	1000	0.912	0.004	0.9678	0.0023	957,886	41	4,533,915	66	957,851	53	4,533,894	78
Mt. Cameroon	92	0.50	94	1000	0.630	0.017	0.7571	0.0148	519,479	391	465,870	348	519,467	578	465,892	530
Licancubar	30	0.06	96	1000	0.983	0.001	0.9911	0.0007	614,636	11	7,474,514	9	614,660	18	7,474,529	17
Karthala	31	0.38	85	1000	0.531	0.019	0.7011	0.0194	322,439	652	8,701,050	559	321,820	896	8,700,949	849
Ambae	30	0.40	89	1000	0.660	0.015	0.8292	0.0132	159,721	330	8,297,226	440	159,810	425	8,297,044	522
MaunaLoa	30	0.40	87	1000	0.836	0.009	0.9204	0.0059	229,686	789	2,156,092	794	229,425	1014	2,156,527	1156
MaunaKea	30	0.19	91	1000	0.898	0.003	0.9753	0.0017	241,421	370	2,191,607	567	241,246	537	2,190,513	1066
Hualalai	30	0.50	92	1000	0.903	0.004	0.9609	0.0020	203,062	466	2,178,379	292	203,287	581	2,178,266	415
Kohala	30	0.40	82	1000	0.690	0.014	0.8503	0.0101	215,566	561	2,223,794	550	215,610	545	2,223,851	596

Note: Grid res. refers to DEM resolution in meter. N. Points refers to the number of points randomly sampled over each delimited region for each of the 1000 runs. Mean r-squared refers to the average of the 1000 r-squared resulting from the Linear Regression method (LR). Std.Dev. r-squared refers to the standard deviation of the 1000 r-squared. Same for Mean Spearman Rho and Std.Dev. Spearman Rho from the Spearman correlation method (SP). X(m) and Y(m) refer to the average coordinates in meter (UTM) of the centers resulting from the 1000 runs using LR and SP methods. Errors are given as 3-sigma errors.

2.3.2. Reconstruction of volcano characteristics and uncertainties

The number and types of original surface points is critical to this analysis and varies among volcanoes. In order to assess the uncertainty this variation engenders, we evaluate several scenarios with different types and numbers of control points (data points on remaining surfaces) for the eleven volcanoes of reference listed in Table 2.

In the first scenario, we used well defined altitudinal profiles with control points radially distributed around the summits. For the five volcanoes Mayon, Licancabur, Fuji, Mt. Somma and Mt. Cameroon, we picked control points (elevations and X, Y coordinates) following detectable lava flows (for Mayon, Licancabur and Fuji), radial directions (for Mt. Cameroon), or remnants topographic ridges that divide drainage areas (for Mt. Somma; Figs. 3, 4, Figs. S1, S2). Such ridges are the less eroded parts on the volcano surface and thus are optimal for the reconstruction of truncated edifices. In addition, in the case of symmetrical geometry, they present a radial organization around the summit (e.g. Karátson et al., 2016) providing excellent altitudinal profiles.

By performing the Linear Regression and Spearman correlation techniques (so called *LR* model and *SP* model, respectively) on these sets of control points, we show, on the one hand, that for the 4 well preserved volcanoes (Mayon, Licancabur, Fuji and Mt. Cameroon), both techniques accurately locate the summits of the volcanoes (Fig. 3, Fig. S1) at a distance of ~10 m to ~200 m from their actual crater (as observed and located on aerial images) and only 10 m to 170 m from each other. Even for the truncated Mt. Somma (Fig. 4), our center locations (*LR* and *SP* models) are only 87 m apart from each other, and are in good agreement with the previous estimations of Cioni et al. (1999) and Favalli et al. (2014).

Along with the location of the center of the long term volcanic activity, our methodology directly estimates the average radial profile of an edifice (Figs. 3, 4, Figs. S1, S2). We show that both *LR* and *SP* methods give similar results on the shape of the 5 volcanoes of reference (distribution of the control points in the DCE diagram for the Mayon, Licancabur, Fuji, Mt. Somma and Mt. Cameroon; Figs. 3, 4; Figs. S1, S2), which suggests that the ordering using linear regression (*LR* method), even for nonlinear general shapes, does not necessarily lead to inconsistencies.

With our approach, the center of the edifice and its general radial shape are given by the center's location that provide the best arrangement in the DCE diagram. For the five volcanoes Mayon, Licancabur,

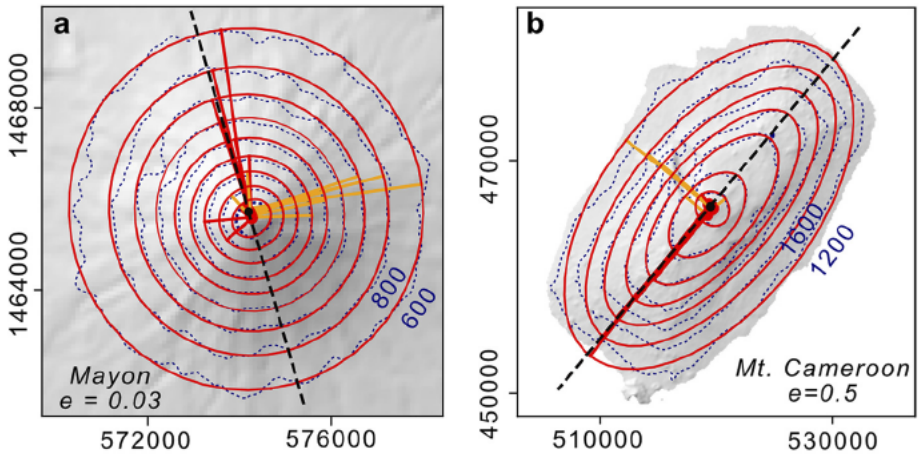

Fig. 2. Ellipticity and symmetry of a volcanic edifice. (a) Hill shaded DEM of the Mayon volcano (UTM zone 51 N, in meters). In blue are shown the 200 m interval contour lines, from 600 to 2200 m elevation. The red concentric forms represent the ellipses that have the same second moment as the region delimited by each contour line. Each ellipse is characterized by its major and minor axes (red and orange straight lines, respectively). The ellipticity *e* of the edifice is given by weighted averaging the ellipticity of each ellipse by their area. The same weighted average of the orientation of all the major axes provides the orientation of the axis of symmetry of the edifice (on the X Y plane, black dashed line). (b) Same as (a) for the Mt. Cameroon (UTM zone 32 N), with 400 m interval contour lines from 1200 m to 3600 m.

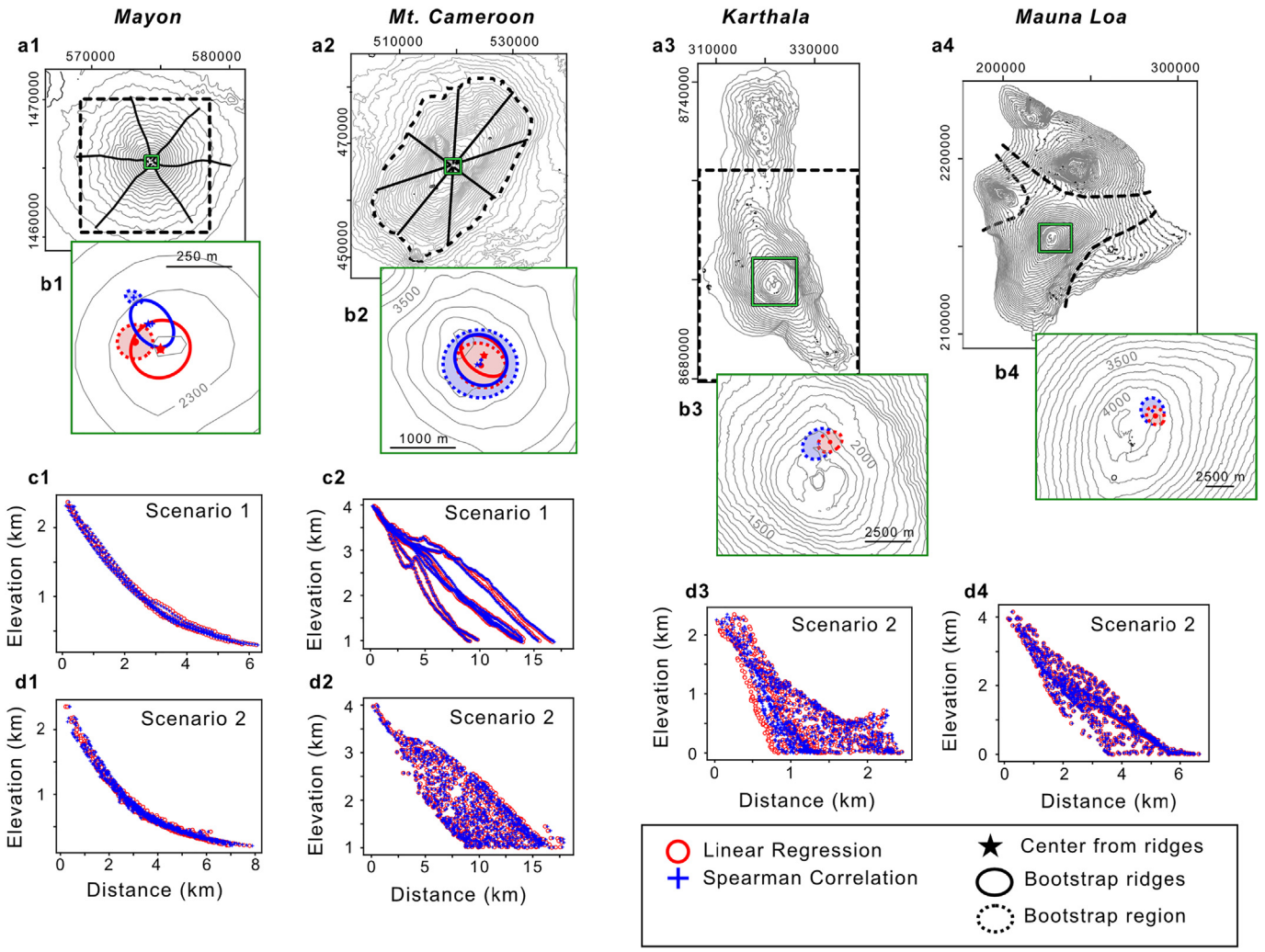

Fig. 3. Case study analysis. (a) Topography of four of the volcanoes used to test the accuracy of the approach: Mayon (UTM zone 51 N, in meters), Mt. Cameroon (UTM zone 32 N), Karthala (UTM zone 38S), Mauna Loaa (UTM zone 5 N). The black lines represent the altitudinal profiles (only for Mayon (a1) and Mt. Cameroon (a2) in this figure). The dashed contours define the region used for the bootstrapping analysis. (b) Zoom on the summits of the volcanoes (green rectangles in (a)). For Mayon (b1) and Mt. Cameroon (b2), the red and blue stars show the reconstructed centers of the edifice estimated using all the control points along the altitudinal profiles, with the *LR* and *SP* methods respectively. The red and blue ellipses show the distribution of 99.7% of the bootstrapping results (see text for details), using half the available points along the altitudinal profiles, for the *LR* and *SP* methods respectively (centers of the ellipses are not reported for better readability). For all the volcanoes (b1–4), the dashed ellipses show the bootstrapping results with 1000 random points selected inside the DEM's delimited regions (in black dashed contours on a1–4). Both *LR* and *SP* methods give similar results over the tested volcanoes, close to the actual craters. (c) General flank profile determined by the *LR* method (in red circle) and the *SP* method (blue crosses) using the altitudinal profiles in (a1–2). (d) Same as (c) but using 1000 points over the delimited regions (dashed contours in a1–4). For every scenario, *LR* and *SP* methods give similar results. See text for details and Tables 1 and 2 for uncertainties.

Fuji, Mt. Somma and Mt. Cameroon, the coefficients of determination (r squared) and the Spearman coefficients of each best arrangement are reported in Table 1 and are close to 1 and close to −1 (due to the anticorrelation) respectively, with p values universally ≪ 0.01. Nonetheless, to test the robustness of our approach and to analyze its sensitivity (i) to the number of control points and (ii) to their spatial distribution, we assessed uncertainties using bootstrapping technique on small sets of control points. We bootstrapped 1000 times with only half of the available control points (distributed along the elevation profile) and estimated the uncertainty of the location of the modeled centers. The 3 sigma errors are given in Table 1 (X and Y directions) and are also reported on Figs. 3 and 4 (and Figs. S1, S2) as ellipses that contains the 997 centers from the 1000 models.

As a further test, and in order to be consistent with the constraints used in previous studies on reconstruction techniques (Karátson et al., 2010; Favalli et al., 2014), we applied the bootstrap methodology (1000 models) after randomly selecting 1000 control points in delimited regions of the volcanoes' DEMs without of following predefined altitudinal profiles (Figs. 3, 4, Figs. S1, S2). We applied this second scenario on the five previous volcanoes and on six other irregular edifices that present ellipticity from 0.18 to 0.50 and a degree of symmetry from 81 to 90% (listed in Table 2). For all these volcanoes, the sampling areas correspond to regions used in a previous study (Favalli et al., 2014) and to regions delimited by geological and topographic constraints (i.e. delimited with the lava flow of the different volcanoes or/and by the topography of the adjacent edifices). Note that all the areas of sampling are larger than the region used to estimate ellipticity and symmetry (since ellipticity needs closed contour lines to be calculated), which may introduce more irregularity for each landform under investigation. Results are shown in Figs. 3 and 4 (and Figs. S1, S2) and the uncertainties are reported in Table 2. We show that even for irregular and asymmetric edifices, our method is able to provide a very good estimate of the center locations (i) in good agreement between *LR* and *SP* model, (ii) in good agreement with previous studies, and (iii) in good agreement with the "actual" center of the edifices. We also show that even with a low number of control points (1000), our results are in very good agreement with previous studies using a greater number of points (2×10^3 to ~200×10^3; Favalli et al., 2014).

Finally, we tested our method on 15 additional scenarios (Supp. Information, Fig. S3), from weakly constrained to very weakly constrained

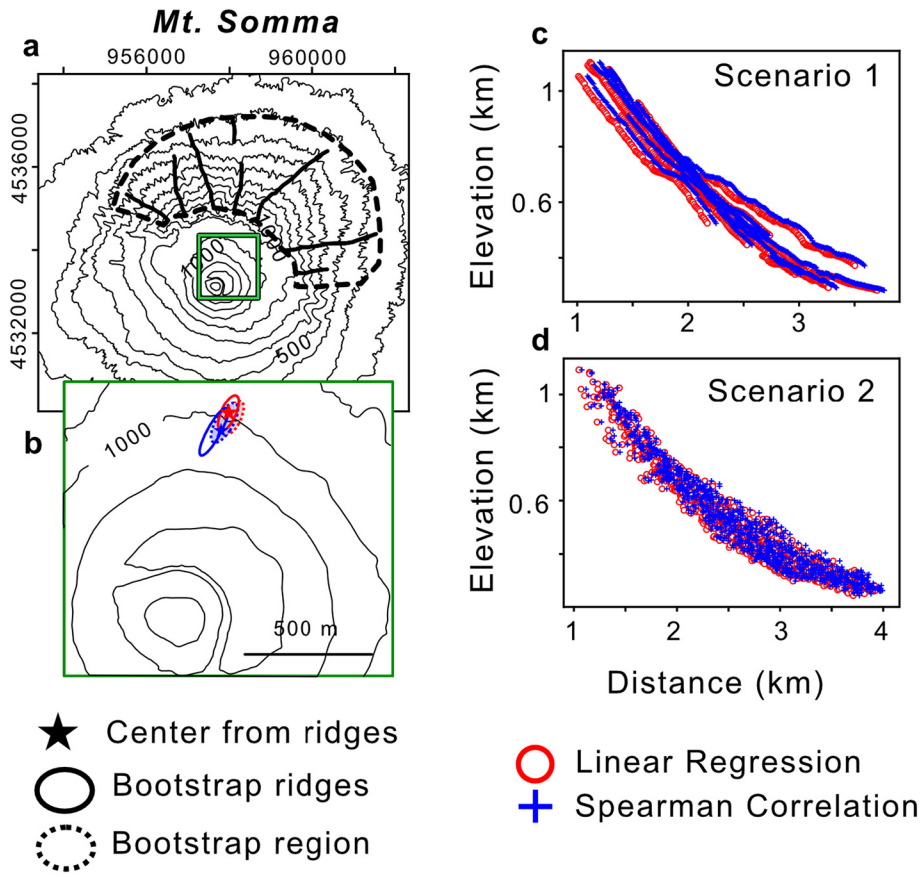

Fig. 4. Case study of a truncated volcano. (a) Topography of Mt. Somma (UTM zone 32 N, in meters). The black lines represent the altitudinal profiles along remnant topographic ridges used in scenario 1 (c). The dashed contour defines the region used for the bootstrapping analysis (same as Favalli et al., 2014). (b) Zoom around the summits of the Mt. Vesuvio represented by the green rectangle in (a). The red and blue stars show the reconstructed centers of the edifice estimated using all the points along the ridges, with the *LR* and *SP* methods respectively. The red and blue ellipses show the distribution of 99.7% of the bootstrapping results, using half the available points along the altitudinal profiles, for the *LR* and *SP* methods respectively (centers of the ellipses are not reported for better readability). The dashed ellipses show the bootstrapping results with 1000 random points selected inside the DEM's delimited regions (in black dashed contours on (a)). Both *LR* and *SP* methods give similar results in good agreement with previous studies (Cioni et al., 1999; Favalli et al., 2014). (c) General flank profile determined by the *LR* method (in red circle) and the *SP* method (blue crosses) using the altitudinal profile along the remnant ridges. (d) Same as (c) but using 1000 points over the delimited regions (dashed line in (a)).

choices of control points, to simulate cases that could be encountered when investigating highly dismantled edifices. Each scenario combines i) three altitudinal ranges: the lower fourth, lower third and lower half part of each volcano with ii) five surface areas: one, two, three quarters, two opposite quarters and four quarters of each volcano. Results of the sensibility analysis show that, as expected, the accuracy of the modeled centers (relative to the "actual" centers) decreases with decreasing altitudinal range and surface area available for constraints, as well as with increasing volcano irregularity (Fig. S3). Nevertheless, for volcanoes with a high degree of symmetry (>95%) and low ellipticity (<0.1), our method performs well for all weakly constrained scenarios, with an average difference between modeled and "actual" centers of 5% of the mean volcano radius. For volcanoes with greater than 90% symmetry (Fuji) and high ellipticity (Mt. Cameroun), the modeled centers are accurate to 6% for all altitude ranges, but only for regions covering all or half of the volcano (two opposite quarters). The deviation rises to an average of 11% of the mean radius of the volcano for Fuji when the smallest portions are used. For irregular volcanoes (degree of symmetry <90%), poor constraints generate inaccurate results (deviation >15%) with strong discrepancies between the modeled *LR* and *SP* centers.

The general shapes of the flanks can only be inferred if the control points available are representative of the flanks they are chosen to elucidate. The accuracy of the profiles, over the range of altitude covered by the constraints, thus mirrors the accuracy of the centers.

3. Application to Réunion Island

3.1. Geological setting

Réunion Island, located 700 km east of Madagascar, is the current active surface expression of the Réunion hotspot that initiated at ~65 Ma with the emission of the Deccan traps (Duncan, 1990). The island is the small subaerial part of a large volcanic system of 220 × 240 km in diameter standing on the ocean floor at 4000 – 4200 m below sea level (bsl). It reaches 3071 m and 2621 m above sea level (asl) at the summits of the dormant Piton des Neiges and the active Piton de la Fournaise volcanoes, respectively (Fig. 5). Altogether the subaerial domains of these volcanoes represent only 3% of the edifice total volume (de Voogd et al., 1999), whose construction started between 5 and 7 Ma ago (Lénat et al., 1989; Gillot et al., 1994).

3.1.1. Volcanic edifices that form the Réunion edifice

Beside Piton des Neiges and Piton de la Fournaise, the presence of two other volcanic structures have been proposed from (i) gravimetric and magnetic data (Malengreau et al., 1999; Gailler and Lénat, 2010), (ii) a deep drill hole on the east coast of Piton de la Fournaise (Lerebour, 1987; Rançon et al., 1989), (iii) radiometric ages (Gillot et al., 1994; Smietana et al., 2010; Smietana, 2011), and (iv) the location and geometry of depocenters inferred for seismic reflection data (Lebas et al., 2018).

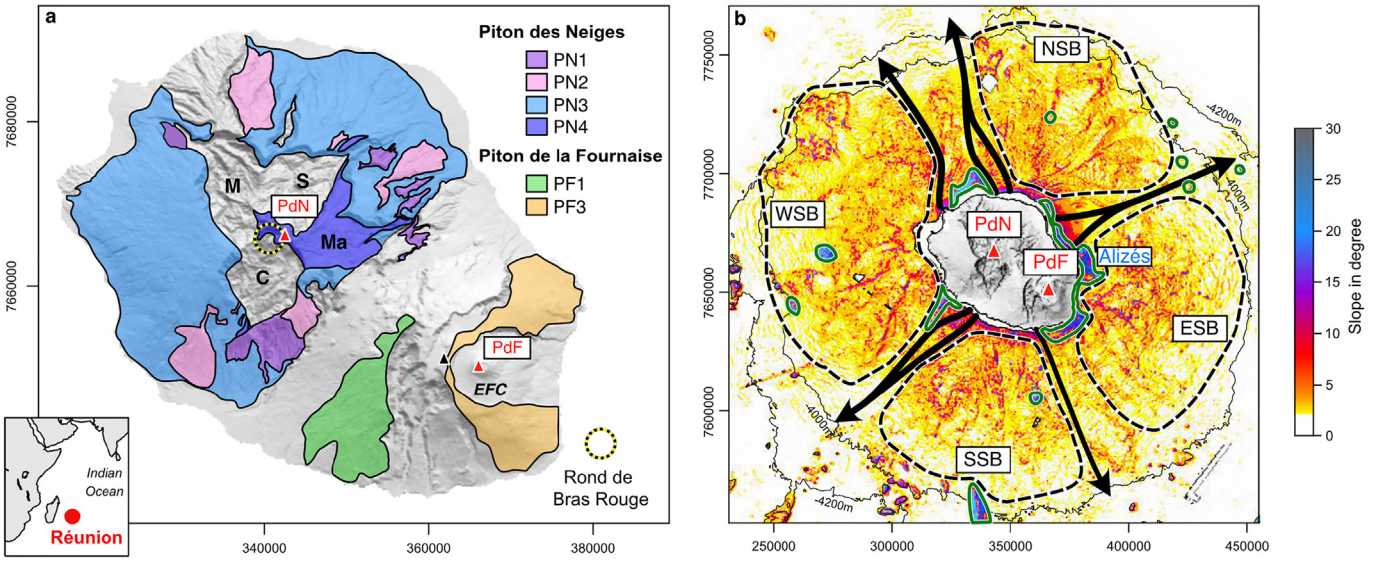

Fig. 5. Subaerial and submarine representation of Réunion Island. (a) Hill shaded Digital Elevation Model of Réunion (25 m resolution, coordinates in meters, UTM zone 40S, © Institut Géographique National -IGN- 1997). M for Mafate cirque, S for Salazie cirque, C for Cilaos cirque and Ma for Marsouins paleo-cirque. The colored patches show the extension of the different remaining surfaces from the different edifices of Piton des Neiges (PdN) and Piton de la Fournaise (PdF) at their different stages of growth (estimated from geomorphogical observations and geochronological dating; McDougall, 1971; Gillot et al., 1994; Salvany et al., 2012). Rond de Bras Rouge is described as the volcanic center of PdN from dyke distribution (Chevallier and Vatin-Perignon, 1982; Chaput et al., 2017). C, S and M denote the erosion structures (cirques) of Cilaos, Salazie and Mafate. The black triangle accounts for the location of the PF1 volcanic center in the Plaine des Sables. EFC: Enclos Fouqué caldera. (b) Slopes map of the submarine topography of Réunion (topo data from the FOREVER and ERODER cruise campaigns) showing the four main bulges (NSB, WSB, SSB, ESB in dashed line, from Labazuy, 1996), the canyons in-between (black arrows), a part of the Alizés volcano, and the sparse volcanic structures on the Réunion submarine flanks. The limit between the deep-sea bottom and the Réunion complex is characterized by the slope transition at around 4200–4000 m bsl.

The most visible sign of an additional volcano is the dense plutonic complex encountered by a deep drill hole (Lerebour, 1987; Rançon et al., 1989) and mapped with gravimetry (Rousset et al., 1989; Gailler and Lénat, 2010) below the east flank of Piton de la Fournaise. This plutonic complex has been interpreted either as an independent dismantled volcano (named "Proto Fournaise" by Lerebour (1987) and "Les Alizés" by Malengreau et al. (1999)), or as the primitive shield volcano of Piton des Neiges and Piton de la Fournaise (Gillot et al., 1994). Lénat et al. (2001) suggested this edifice to have been formed in the Matuyama period, between 0.78 and 2.59 Ma. However, radiometric dates obtained on volcanic rocks dredged 1500 1700 bsl along the submarine NE flank of Piton de la Fournaise yielded the oldest ages of Réunion (3.34 ± 0.07 and 3.77 ± 0.08 Ma; Smietana et al., 2010; Smietana, 2011) compatible with the reversely magnetized Mammoth subchron and Gilbert period, and consequently suggesting that Piton de la Fournaise may have been built on an old (>3 Ma) buried edifice, the spatial extent of which remains unknown.

The existence of a fourth volcano has also been proposed using reflection seismic data that suggest the occurrence of a depocenter below the deposits of Piton des Neiges, slightly north of the current summit of Piton des Neiges (Lebas et al., 2018). Lebas et al. (2018) relates this depocenter to the construction of the Proto Piton des Neiges volcano but with an undetermined age. Altogether, the construction of the Réunion edifice would then result from the activity of four volcanoes.

3.1.2. Succession of building and dismantling periods in the history of Réunion Island

Radiometric dating of volcanic formations reveals that both Piton des Neiges and Piton de la Fournaise volcanoes experienced successive periods of volcanism and lull (McDougall, 1971; Gillot et al., 1994; Salvany et al., 2012). The oldest dated lava flows of Piton des Neiges indicate the emergence of the island before 2.2 Ma (McDougall, 1971; Quidelleur et al., 2010). Since then, five successive edifices have been constructed: La Montagne, and PN1 to PN4 (Salvany et al., 2012; Fig. 5a). Their remains can be identified on the outer subaerial slopes of the massif (Fig. 5a). Magmas emitted until 430 ka (end of PN2) present a fairly constant composition made of basalts and olivine rich basalts of the transitional series, typical of a shield building stage (Peterson and Moore, 1987), whereas differentiated lavas of the alkaline series (hawaiite to trachyte, classically associated with the post shield stage) were produced and emitted during the volcanic periods that constructed PN3 and PN4 (i.e. post 340 ka; Fig. 5a; Upton and Wadsworth, 1966). The occurrence of plagioclase ultraphyric lava flows accumulated vertically over several hundreds of meters since 340 ka (Kluska, 1997) was recently interpreted as related to decreasing magma supply from depth until the last limited eruptions around 30 ka ago (Valer et al., 2017).

The known evolution of Piton de la Fournaise is significantly shorter than that of Piton des Neiges. The oldest lavas attributed to Piton de la Fournaise date back to 527 ka (Gillot et al., 1994) and reflect differentiated magmas of alkaline affinity similar to the ones emitted by Piton des Neiges volcano during PN3 and PN4 periods (Albarède et al., 1997). Around 395 ka, the magma composition shifted toward mafic lavas identical to the ones emitted by Piton des Neiges before 430 ka (Albarède et al., 1997). Then, lava flow accumulation between 395 and 290 ka led to the building of a main volcanic cone, PF1, whose remnant corresponds to the southwestern slopes of Piton de la Fournaise (Fig. 5a; Gillot et al., 1994). At around 290 ka, the edifice experienced a major flank landslide that triggered the dismantling of the east part of the volcano and the emplacement of debris avalanche deposits in the submarine domain (Duffield et al., 1982; Oehler et al., 2008; Le Friant et al., 2011). A new volcanic period started around 130 150 ka after a period of low volcanic activity and erosion (Mairine and Bachèlery, 1997), but the geometry of the newly built edifice (PF2) is uncertain due to limited paleo surfaces and to scattered radiometric ages (Gillot et al., 1994). Piton de la Fournaise then experienced a second large landslide around 45 60 ka that was followed by the reconstruction of a third edifice (PF3) whose flanks correspond to the current volcano outside the Enclos Fouqué caldera (Fig. 5a; Gillot et al., 1994). The flanks of this edifice have only been slightly resurfaced by a few lava flows since the collapse of this summit structure (Albert et al., 2020).

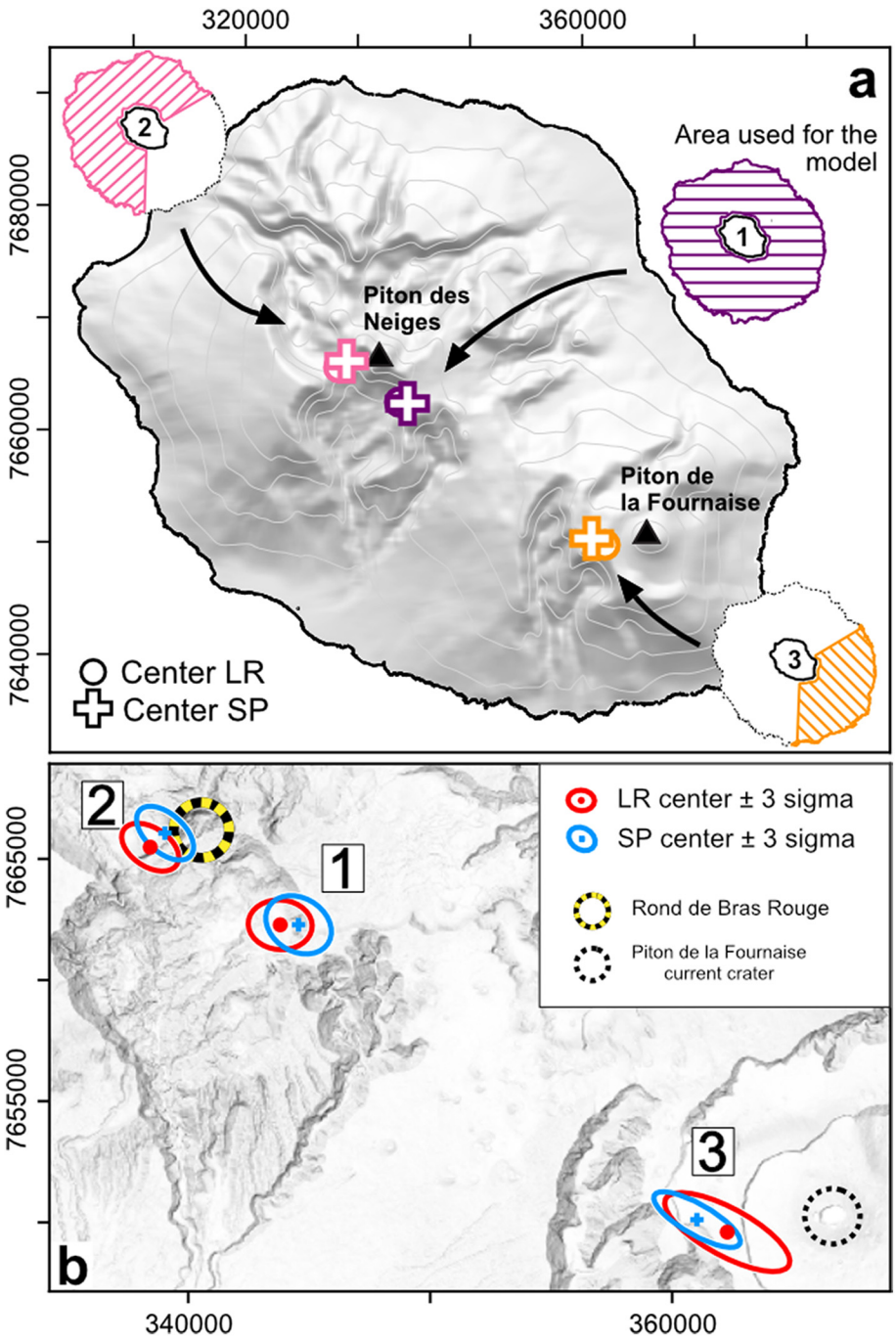

Fig. 6. Center of the edifice of Réunion from the submarine part. (a) Hill shaded DEM of Réunion (150 m resolution, coordinates in meters, UTM zone 40S). Circle and cross show the location of the reconstructed center of the edifice with the *LR* and *SP* methods, respectively. In purple, the locations of the center of the edifice reconstructed from 1000 models using 1000 control points randomly picked over the entire submarine area around Réunion (between 4000 m bsl and 0 m, purple hatched area #1). In pink the results from models using only control points in the area associated with Piton des Neiges (pink hatched area #2). In orange the results using control points in the area associated with Piton de la Fournaise (orange hatched area #3). (b) Zoom on the top of the island (hill shaded DEM 25 m resolution, coordinates in meters, UTM zone 40S) showing the difference between the spatial distribution of the 1000 centers resulting from the *LR* (in red) and from the *SP* (in blue) methods for the area 1, 2 and 3. Ellipse represent the 3-sigma errors on the 1000 centers. The *LR* and *SP* methods give very consistent results despite the chaotic surfaces of the submarine flanks.

3.1.3. Location of the volcanic centers

The evolution of Piton des Neiges and Piton de la Fournaise is marked by the superposition of successive volcanic edifices that can be associated, through time, with the migration of volcanic centers. For Piton des Neiges, migration of the centers has been invoked to explain the elongated shape of the large plutonic body centered on the volcano (Malengreau et al., 1999). However, the distribution of the magmatic intrusions suggests constant magma pathways through time (like the Etang Salé and N120 rift zone), and consequently suggests a stable volcanic center from PN1 to PN4, located in Rond de Bras Rouge (Fig. 5a; Chevallier and Vatin Perignon, 1982; Chaput et al., 2017).

In the case of Piton de la Fournaise, the radial distribution of the dyke swarms related to PF1, the abundance of plutonic cumulates in the lavas emitted in the Plaine des Sables and the gravity anomaly below this area evidence an initial location of the volcanic center 5 km west of the

current summit (Fig. 5a; Duffield et al., 1982; Bachèlery and Mairine, 1990; Gailler and Lénat, 2010; Merle et al., 2010; Michon et al., 2016). The migration of the volcanic center PF1 toward its present location likely occurred after the flank landslide that affected PF2 and led to the abandonment of the SW rift zone that was active during PF1 and PF2 (Bachèlery et al., 2006; Merle et al., 2010; Michon et al., 2016). Whether the migration of the volcanic center results from, or is the cause of, the flank landslide is still debated (Duffield et al., 1982; Gillot et al., 1994; Gailler and Lénat, 2010; Michon et al., 2016).

3.1.4. Structure and nature of the submarine flanks

The submarine flanks of Réunion Island present a complex morphol ogy, controlled by the nature of the rocks and the emplacement pro cesses (Fig. 5b). Three main structures can be identified: bulges, canyons and volcanic structures (e.g. volcanic cones and lava flow accu mulation). The bulges are the main extended features with an overall fan shape geometry and a chaotic topography with slopes from 2 to 10° (Fig. 5b). Previous studies have identified four main submarine bulges around Réunion that have been interpreted as the result of dis mantling processes such as volcano spreading (Le Friant et al., 2011) or flank landslides (Labazuy, 1996; Lénat et al., 1989; Oehler et al., 2008). The west, north and south submarine bulges have been related to Piton des Neiges evolution while the east one is associated with Piton de la Fournaise (Fig. 5b). Moreover, Gailler and Lénat (2010) pro posed that the western and eastern bulges, made of breccias, would to tally cover offshore extensions of volcanic constructions. Between each bulge large submarine canyons developed, connecting the main water sheds to volcaniclastic sedimentary fans in the abyssal plain (Fig. 5b; Saint Ange et al., 2011; Babonneau et al., 2013; Mazuel et al., 2016), and enabling an efficient source to sink dynamics in a context of in tense erosion (Salvany et al., 2012; Gayer et al., 2019). Finally, uneven structures built by submarine lava flows can also be found to a more limited extent. These features present steep slopes (>15°) and are lo cated either in the continuity of the rift zones of Piton de la Fournaise and Piton des Neiges or on the submarine flanks forming independent volcanoes (Fig. 5b; Michon et al., 2016).

3.2. Results

The subaerial portion of Réunion represents only a small fraction of volume of the total structure that rises from the seafloor (~4200 m bsl) to ~3000 m above sea level. In order to better understand the evo lution of the voluminous complex it is necessary to characterize features such as center(s) of eruption and general shape(s) of both subaerial and submarine parts of the volcanic body.

3.2.1. Center reconstructed from submarine domain

Volcanic islands, like other volcanic edifices experience destruction through erosion, flank collapse or volcanic spreading. When such deg radation processes affect subaerial edifices, the products are brought off shore by the rivers, or directly through gravity flows (e.g. Saint Ange et al., 2013).

The marine topography of a volcanic island is thus the result of (i) aggradation by construction, (ii) destruction by deformation when it

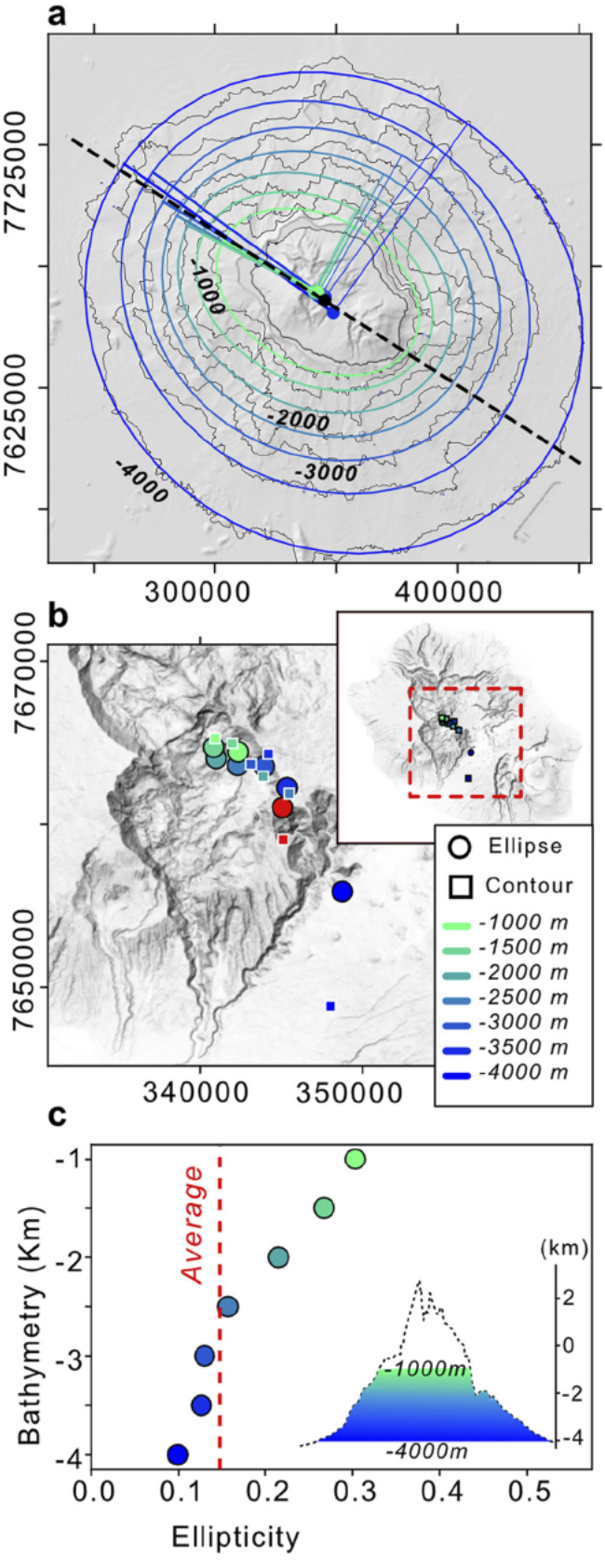

Fig. 7. Ellipticity of the submarine part of Réunion. (a) Hill shaded DEM of the submarine topography of Réunion (topo data from the FOREVER and ERODER cruise campaigns). 1000 m interval contour lines are shown in black. For each contour line from 4000 to 1000 m, the ellipse with the same second moment of the area of the closed contour line is shown in color (blue to green). The major and minor axis of the ellipses are also represented in color and the averaged orientation (weighted by the ellipses areas) of the major axis is given by the dashed black line which represents the plane of symmetry of the edifice from 4000 to 1000 m bsl. (b) Zoom on Piton des Neiges and comparison of the location of the centroids calculated from the actual contour lines (square) and the centroids of the ellipses (circles). Centroids are only up to 2 km apart (except for the 4000 contour lines with 5 km) indicating that the modeled ellipses are good representation of the ellipticity of the edifice. The red circle represents the location of the centroid weighted by the area of the different ellipses, the red square the centroid weighted by the area of each contour line. (c) Evolution of the ellipticity *e* of the edifice between 4000 and 1000 m bsl, calculated from the modeled ellipses in (a). In red is reported the weighted average of the ellipticity (weighted by the area of each ellipse).

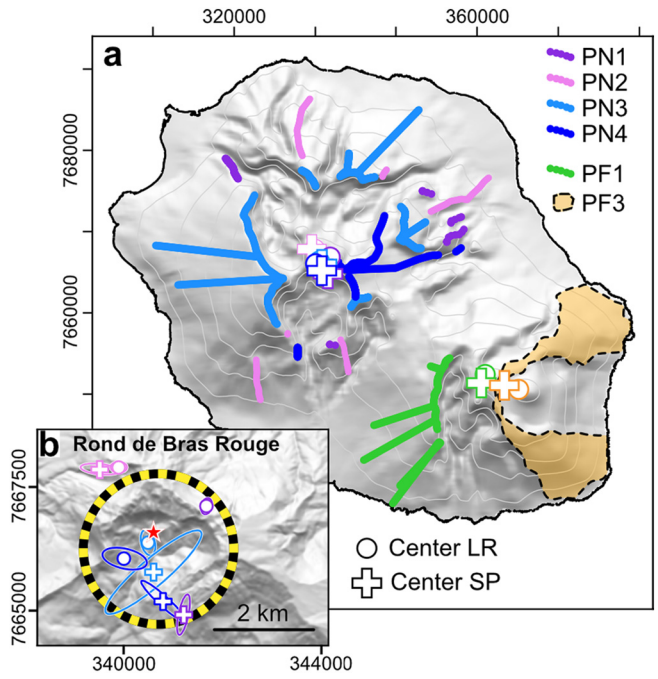

Fig. 8. Location of the reconstructed eruption centers of Réunion Island. (a) Hill shaded DEM of Réunion (150 m resolution, coordinates in meters, UTM zone 40S). Colored circles show the profiles of control points used to reconstruct the centers of eruption and the general flank shapes of Piton des Neiges and Piton de la Fournaise at their different stages of growth (PN3 and PN4 from Gayer et al., 2019). For each edifice, both *LR* (circle) and *SP* (cross) methods show very similar results. (b) Zoom in Rond de Bras Rouge area and the summit of Piton des Neiges, showing how close are the reconstructed centers of the reconstructed PN1, PN3 and PN4, all located in Rond de Bras Rouge (or next to it for the PN1 *SP* method and for PN2). For PN1, PN2, PN3 and PN4, *LR* and *SP* results are 1.8, 0.4, 0.5 and 1.2 km apart, respectively. Colored ellipses represent the 3-sigma errors when resampling 500 control points 1000 times.

exists, and (iii) aggradation of the products of this destruction and erosion. However, to a first order, one can consider that submarine flanks of a volcanic island are controlled by slope stability. Thus, the topography of submarine flanks can be leveraged as if they were surfaces of a volcanic edifice and therefore, can be used to reconstruct the features of the whole volcanic structure.

Around Réunion, bathymetry data show a slope transition occurring between 4000 and 4200 m bsl (Fig. 5b), suggesting the volcanic structure to start at approximately 4000 m bsl. Using only the bathymetric data between 4000 m bsl and sea level (i.e. without considering aerial topographic data sets), we applied our methodology to estimate the location of the center of the complex. We carried out 1000 models from 1000 control points randomly picked around Réunion, in order to evaluate the uncertainties related to the roughness of the submarine domain. With both *LR* and *SP* methods, the resulting centers are located approximately 5.5 km southeast of the Rond de Bras Rouge, an area previously identified, from geological data, as the long term eruptive center of Piton des Neiges (Fig. 6; Chevallier and Vatin Perignon, 1982; Chaput et al., 2017). In addition, these centers are only ~800 m apart from each other and the 3 sigma errors on 1000 runs with 1000 points are only 1 to 1.3 km. Our results are also very close to the averaged centroid of the structure, derived from the available closed contour lines between 4000 and 1000 m bsl, which we used to estimate the weighted mean ellipticity *e* of the edifice of 0.15 (Fig. 7). The ellipticity of each contour line (every 500 m) ranges between 0.1 and 0.16 between 4000 and 2500 m bsl and significantly increases above 2500 m bsl to reach 0.32 at 1000 bsl (Fig. 7c).

3.2.2. Reconstruction of the volcanoes characteristics from subaerial parts

Piton des Neiges and Piton de la Fournaise are the two subaerial volcanoes that shape Réunion Island. Remnants of the different growth stages of Piton des Neiges are well preserved on the island's northern and western parts, while the currently active Piton de la Fournaise forms the southeastern part of the island (Fig. 5a; McDougall, 1971; Gillot et al., 1994; Salvany et al., 2012). In a previous study, we used the general concept of the method presented in this paper to reconstruct the Piton des Neiges edifices at its two last stages of growth, i.e. PN3 and PN4 (Gayer et al., 2019). Here, we combine radiometric dates and the location of the different surfaces of Piton des Neiges, as well as topographic ridges to investigate the geometric features of the Piton des Neiges at its precedent stages of growth, PN1 and PN2, and we update our previous results with uncertainties. Figs. 8 and 9 illustrate the overall evolution of Piton des Neiges (from PN1 to PN4), and these results are summarized in Table 3.

Most of the surfaces of PN1 and PN2 have been covered by younger lava flows and/or have been eroded. However, remnants dated at around 950 1200 ka for PN1 and 430 660 ka for PN2 (Salvany et al., 2012) are located on the outer parts of the edifice (Figs. 5a and 8a). The least eroded ridges of PN1 are to the North and East of Piton des Neiges, and range from 50 to 1850 m asl in elevation, which likely corresponds to an intermediate portion of the original structure and is more than one third the size of the present structure. On PN2, the least eroded ridges are in a similar orientation from Piton des Neiges and from 90 to 1940 m asl from the base to two thirds of the present structure. Using these remnants, admittedly of limited representativeness (especially for PN1), we modeled the

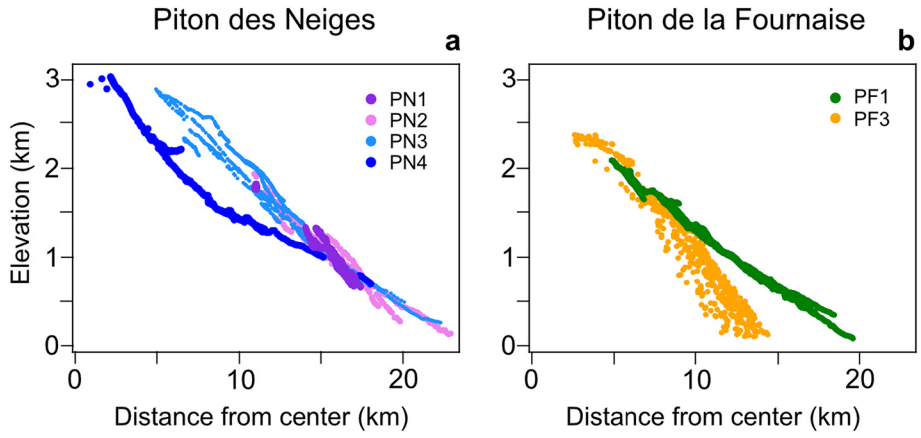

Fig. 9. General flank profiles of the reconstructed edifices of Réunion. (a) General shape of the flanks of PN1, PN2, PN3, and PN4 from the *LR* method (*LR* and *SP* methods results are shown together in the Fig. S2; PN3 and PN4 are from Gayer et al., 2019). PN1, PN2 and PN3 show close geometries. PN4 shows a flank shape with changing slope, with an elevation interpreted to be ~3400 m (Gayer et al., 2019). (b) General shape of the flanks of PF1 and PF3 from *LR* method (*LR* and *SP* methods results are shown in the Fig. S2). Color code for (a) and (b) is the same as in Fig. 8.

Table 3
Coordinates (UTM Zone 40S) of the centers estimated for the different stage of Piton des Neiges (PN) and Piton de la Fournaise (PF).

Volcano	r-Squared	Spearman Rho	Profiles					Bootstrap on profiles							
			N. points	Center LR		Center SP		N. points	Center LR				Center SP			
				X(m)	Y(m)	X(m)	Y(m)		X(m)	±	Y(m)	±	X(m)	±	Y(m)	±
PN1	0.97	0.987	1282	341,671	7,667,102	341,205	7,664,907	500	341,672	57	7,667,101	111	341,207	130	7,664,910	407
PN2	0.96	0.988	1083	339,925	7,667,858	339,566	7,667,819	500	339,923	167	7,667,859	109	339,543	384	7,667,822	113
PN3	0.94	0.975	12,299	340,505	7,666,362	340,832	7,665,950	500	340,507	149	7,666,355	256	340,614	962	7,665,764	837
PN4	0.96	0.997	5006	340,046	7,666,028	340,851	7,665,152	500	340,040	445	7,666,034	219	340,819	451	7,665,182	413
PF1	0.99	0.999	3767	361,018	7,652,403	360,578	7,651,412	500	361,022	617	7,652,397	262	360,620	653	7,651,486	545
								Bootstrap on delimited regions								
								N. points	**Center LR**				**Center SP**			
									X(m)	±	**Y(m)**	±	**X(m)**	±	**Y(m)**	±
PF3								1000	364,994	208	7,650,585	91	363,341	649	7,651,128	178

Note: * For Profiles: N. Points refers to the number of points of the altitudinal profile. r-squared and Spearman Rho refer to the r-squared and Spearman Rho of the LR and SP methods using all the points on profile, respectively. X(m) and Y(m) refer to the coordinates in meter (UTM Zone 40S of the resulting centers using LR and SP methods). * For Bootstrap on Profiles: N. Points refers to the number of points randomly sampled over each profile for each of the 1000 runs. X(m) and Y(m) refer to the average coordinates in meter (UTM Zone 40S) of the centers resulting from the 1000 runs using LR and SP methods. Errors are given as 3-sigma errors. * For Bootstrap on Delimited region: N. Points refers to the number of points randomly sampled over the delimited region for each of the 1000 runs. X(m) and Y(m) refer to the average coordinates in meter (UTM) of the centers resulting from the 1000 runs using LR and SP methods. Errors are given as 3-sigma errors.

eruptive centers of PN1 and PN2 and found they fall within or on the edge of Rond de Bras Rouge (Fig. 8) in good agreement with previous estimates of PN3 and PN4 (Gayer et al., 2019) and consistent with the distribution of dykes that point to this same location (Chevallier and Vatin Perignon, 1982; Chaput et al., 2017). Uncertainties of the location of all the centers of PN1, PN2, PN3 and PN4 were estimated using the bootstrap technique described in Section 2.3.2, with 1000 models using 500 points along the respective profiles. *LR* and *SP* centers are only 0.3 to 1.9 km apart from each other when using all the points available on the different profiles, and 3 sigma errors are only of 60 to 900 m when resampling only 500 points (on 1000 runs). In the DCE diagram (Fig. 9a, Fig. S4), the distribu tion of control points indicates that the flanks of PN1, PN2, and PN3 are superposed for the altitudinal ranges covered by the remnants. Combin ing the results of the *LR* and *SP* methods, the DCE diagram suggests that PN1, PN2, and PN3 were characterized by flanks with an average slope of ~9 10°, above 500 m elevation (Fig. 9a; Fig. S4). Despite the limited al titudinal extent of the constraints for PN1, the consistency of the location of the centers and the superposition of the general profiles of PN1, PN2, and PN3 provide support for the PN1 model results.

For Piton de la Fournaise, we used the remnant surfaces dated at 290 ka (Fig. 4a) to constrain the center of eruption and the general shape of PF1. We estimate an eruptive center located ~6 km west of the current crater (Fig. 8a), and both *LR* and *SP* methods are consistent with inde pendent geological evidences (Bachèlery and Mairine, 1990; Merle et al., 2010; Michon et al., 2016). The DCE diagram suggests the general shape of PF1 has an average slope of ~8 9° below 1500 m elevation (Fig. 9b; Fig. S4). For PF3, based on the region attributed to this edifice (Fig. 8), we performed 1000 models with 1000 randomly picked control points. The centers resulting from the *LR* and *SP* methods are only 1.7 km apart (Table 3) and are located between the center of PF1 and the current crater (Fig. 8a). This result is in excellent agreement with the chronology of construction of Piton de la Fournaise (Letourneur et al., 2008; 3 sigma errors are of 90 to 650 m; Table 3). Finally, the flank pro file of PF3 shows (with both *LR* and *SP* methods) a slope of ~14° below 1500 m asl that flattens above 2000 m asl (Fig. 9b; Fig. S4).

It should be noted that the consistency between the results of the *LR* and *SP* methods depends on both the number of control points and on the regularity of the surface they intend to represent. Therefore, the dis tribution of the control points in the DCE diagram are not expected to be always aligned between the *LR* and *SP* methods. Consequently, a slight offset, as obtained for the PN1, PF1 and PF3 (Fig. S4) should be used to estimate uncertainties on the 3D surfaces one would seek to reconstruct from the features revealed by our approach. As for stronger differences, the implications are discussed in the next section.

4. Discussion

4.1. Volcano characteristics reconstruction

The accuracy of any reconstructed volcanic morphology, by any technique, depends on few key factors such as (i) how pre erosion sur faces are constrained (in the case of dismantled edifices), (ii) the critical number and the geographic distribution of control points (both for re constructions on dismantled volcanoes and for reconstructions on well preserved volcanoes) and (iii) the symmetry of the volcanic land form under investigation.

The method presented in this paper is as sensitive to these factors as other techniques, and therefore, it does not offer a path toward more ro bust characterization of highly irregular surfaces or from surfaces with few control points. Nonetheless, our method, based on the coupling of two simple mathematical techniques, allows us to efficiently test the consistency of the results with respect to the key factors that control the accuracy of the reconstruction. For example, a significant difference in the two locations of the reconstructed centers (resulting from the *LR* and *SP* methods), and consequently, a significant difference in the two mean radial shapes, can be interpreted as being related either to control points limited in altitude, or to the fact that the landform is too irregular to be assimilated to a simple concentric geometric shape. We believe that a major difference between the *LR* and *SP* centers should be interpreted as a deficit of constraints since we show that our method is able to estimate the center of long term eruptive activity of irregular volcanoes with only few differences between the *LR* and *SP* center's lo cations. In the particular case of an irregular edifice with consistent *LR* and *SP* centers, it is possible to quantify the extent of asymmetry of the edifice by analyzing the average radial shape in a DCE diagram. While a narrow point cloud demonstrates the regularity and symmetry of an edifice, a spread out scatterplot indicates a noncircular and/or asymmetric volcanic landform that cannot be modeled with a concen tric geometry.

While our approach does not allow a 3D reconstruction of a volcanic surface, it provides a quick, simple and efficient method for providing two key inputs to such reconstructions: the location of the volcanic cen ter and the average shape of the surface within the altitudinal range covered by the constraints. Like other methods, it performs best when the surface is conical. However, and while our method does not provide a direct tool to model irregular shapes, it is worth noting that for elon gated edifices with two symmetry axes (and a degree of symmetry >85%), the envelope of the scatterplot (in the DCE diagram) can be used to determine the mean radial shape along the minor and major

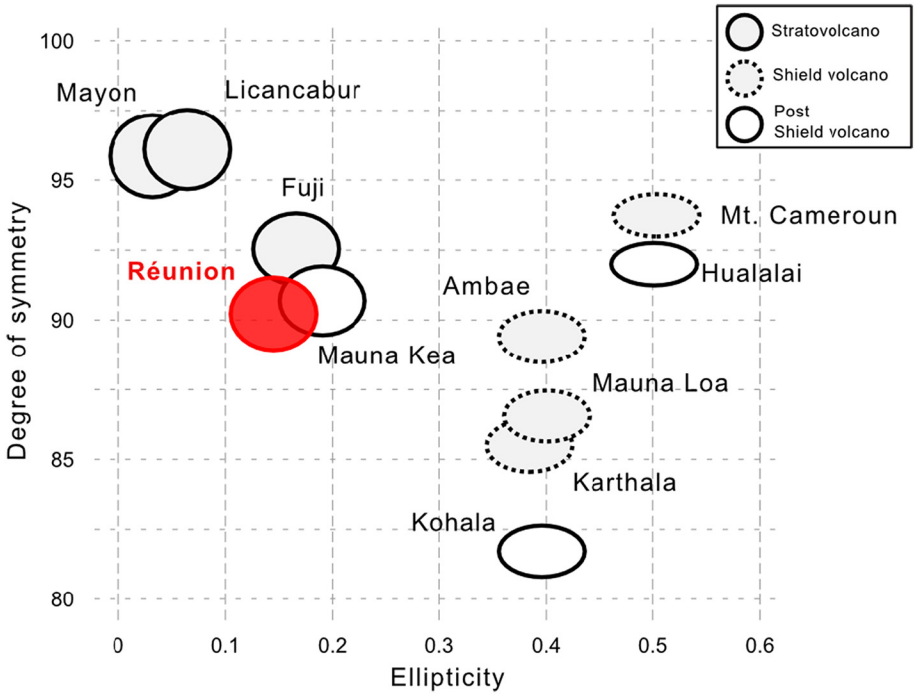

Fig. 10. Range of applicability of the method. Ellipticity vs. Degree of symmetry of the ten edifices used in Section 2, and of the submarine edifice of Réunion (between 4000 and 1000 m bsl). Ellipticity is defined as $e = (a \quad b) / a$ where a and b are the major and minor axis of an ellipse respectively. See text for detail on the estimate of the degree of symmetry.

axis, and thus can be used for the modeling of the 3D surface that best fits the landform under investigation.

4.2. Relative significance of Piton des Neiges and Piton de la Fournaise

Réunion Island has an elliptical shape due to the juxtaposition of the two well defined volcanoes Piton de la Fournaise and Piton des Neiges (Fig. 5a). However, the base of the whole volcanic complex at 4000 m bsl does not show any pronounced oblong shape ($e = 0.1$, Fig. 7) and has been described instead as a circular edifice (Le Friant et al., 2011). Although the geometry due to the juxtaposition of the two volcanoes is not preserved down to the sea floor, the submarine flanks of the com plex show bulges that result from the dismantling of the two subaerial volcanoes covering the actual volcanic structure (Gailler and Lénat, 2010; Fig. 5). The eastern bulge has been associated with Piton de la Fournaise while the three others (northern, western and southern) were associated with Piton des Neiges (Labazuy, 1996; Oehler et al., 2008; Le Friant et al., 2011; Fig. 5b). Based on this spatial distribution, we used our approach to estimate the center of (i) a potential volcanic complex described only by the eastern part of the submarine flank of Réunion Island and (ii) a potential volcanic complex described by the three others northern, western and southern bulges. On the one hand, using the eastern part of the submarine flanks, both *LR* and *SP* methods locate the center of the edifice 6 km west of the present crater of Piton de la Fournaise and 1 km south of that of PF1 (Fig. 8). On the other hand, using the submarine flanks on the northern, western and southern part of the island, both *LR* and *SP* methods locate a center next to Rond de Bras Rouge (1.5 km west; Fig. 6). These estimates are very consistent with the reconstructed centers of Piton des Neiges and Piton de la Fournaise calculated from the subaerial parts of the two volcanoes (Fig. 8). It confirms that the eastern bulge is directly related to the Piton de la Fournaise and that the other three are only related to the Piton des Neiges. Such a spatial distribution would suggest that the Piton des Neiges is the dominant structure of the whole complex,

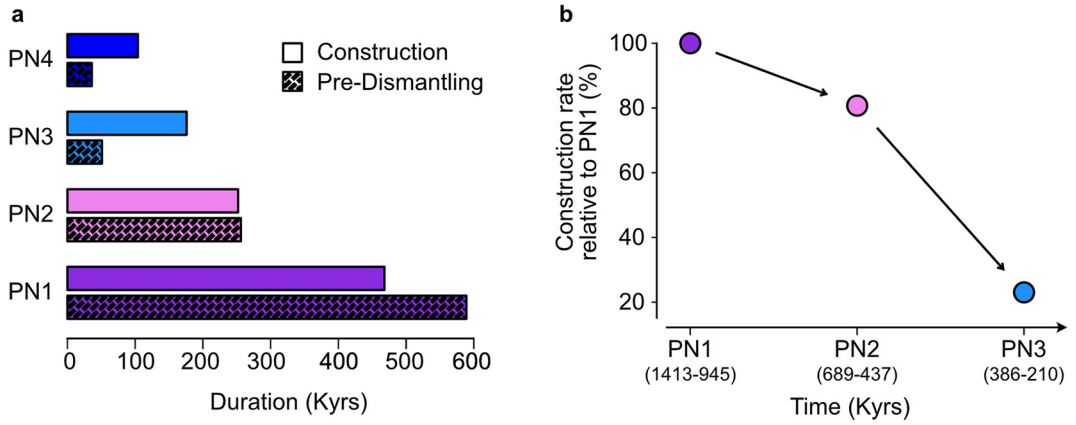

Fig. 11. Duration and rate of construction of Piton des Neiges. (a) represents the duration of construction (Dcn in Eq. (2)) and the duration of the preceding dismantling (pre-dismantling, Ddn-1 in Eq. (2)) for each stage in the history of the Piton des Neiges (ages taken from Salvany et al., 2012). (b) Construction rates of PN1, PN2 and PN3 normalized to the rate of PN1 (see text for details).

as confirmed by the position of the reconstructed center when using the entire submarine domain (with no distinction between the eastern bulge and the others; case 1 in Fig. 6). Indeed, this center is close to Rond de Bras Rouge (case 1 in Fig. 6), which implies that the whole com plex is mainly composed of the Piton des Neiges and that Piton de la Fournaise, a smaller edifice, may have actually developed on the eastern flank of Piton des Neiges.

This result may be further constrained by the analysis of the evo lution of the ellipticity of the submarine domain with depth. Elliptic ity range from 0.1 to 0.32 between 4000 and 1000 m bsl and the centroids of the isobath are clustered near Piton des Neiges except for the isobath 4000 m bsl (Fig. 7). This can be explained by the fact that the base of the whole volcanic complex is not at the same depth, but at 4200 and 3800 m bsl at the base of the northwest and southeast flanks, respectively (Fig. 5b). Consequently the 4000 m bsl isobath includes an abyssal domain in the southeastern part, which results in a centroid located in an almost equidistant position of Piton des Neiges and Piton de la Fournaise (Fig. 7a, b). At shallower depth, the 3500 and 3000 m bsl contours, which are limited to the submarine edifice, are characterized by a slight ellipticity (e ~ 0.13) and by centroids located at the same place as the center we deter mined for the entire submarine domain (methods *LR* and *SP*, case 1 in Fig. 6). Finally, the isobaths from 2500 to 1000 m bsl, show an in crease in ellipticity, which can be explained by the combined effect of the constructions of the Alizés and Piton de la Fournaise in the south east, and by the western bulge of Piton des Neiges, whose volume has been increased by the last destabilizations of the main flank of the volcano between PN2 and PN3 (Bachèlery et al., 2003).

By taking into account the entire complex of Réunion Island (subma rine and aerial domains), our morphological analysis shows that the en tire complex is mainly composed of the Piton des Neiges and that neither the Piton de la Fournaise, a smaller edifice, nor Les Alizés, a bur ied edifice, have significantly influenced the general shape of the Piton des Neiges.

Moreover, the regularity of the PNs (as indicated by the control point distribution in the DCE diagram; Fig. 9) and to a lesser extent that of the PFs, suggest that their growth was not significantly influenced by pre existing structures and, consequently, that the products of Piton des Neiges and Piton de la Fournaise volcanoes almost entirely covered the edifices that preceded them (i.e. the Proto Piton des Neiges and Alizés volcanoes). Indeed, the only identified outcropping relics related to these ancient volcanoes are the rare submarine lava flows off the NE coast of Piton de la Fournaise (Fig. 5b). This suggests that whenever the old volcanoes were built, they were sufficiently small or dismantled to be hidden or locally draped later by Piton des Neiges and Piton de la Fournaise. It also reveals that magma emission related to the different volcanoes remained at the same location despite the ~100 km north eastward shift (Muller et al., 1994; Kreemer, 2009) of the lithosphere since 3.77 Ma (i.e. minimum age of the volcanism that builds the edifice of Réunion; Smietana, 2011).

4.3. Implications of the reconstructed volcanoes characteristics on the evo lution of Piton des Neiges and Piton de la Fournaise

4.3.1. Volcanic center migration

By reconstructing the centers of the successive Piton des Neiges (PN1 to PN4) from remnants covering a wide range of ages, we show that their location did not change significantly during the past 1.4 million years (Fig. 8). The geographical stability of Piton des Neiges is also highlighted by the fact that the center estimated from the submarine flanks is in close agreement with the observed centers of the subaerial volcanoes (PN1 to PN4; Figs. 6, 8). This, sug gests that if the elongated shape of the large gravity anomaly below Piton des Neiges reflects a volcanic center migration (Malengreau et al., 1999), this shift occurred before 1.4 Ma (i.e. PN1). Thus, the re sults of our simple approach agree with the geological data from previous studies (Chevallier and Vatin Perignon, 1982; Chaput et al., 2017). Conversely, our reconstructions confirm that the volcanic center of Piton de la Fournaise experienced a progressive migration between PF1 and PF3 (3.5 km) and between PF3 and its current loca tion (1.5 km) for a total of about 5 km of eastward shift over the last 0.5 Ma (Fig. 4). This migration has previously been attributed to large eastward slumps or flank collapses, favored either by the growth of Piton de la Fournaise on the eastern slope of Piton des Neiges or by hyaloclastites or hydrothermal layers (Duffield et al., 1982; Merle and Lénat, 2003; Letourneur et al., 2008). Such a migration of the vol canic center after flank landslide would then be similar to that ob served in Tahiti Nui (Hildenbrand et al., 2004) suggesting that large flank landslides that cut the magmatic center favor the migra tion of the latter. In turn, the stability of the volcanic center of Piton des Neiges since 1.4 Ma would suggest that this volcano, since then, did not experience large flank collapse as suggested by Salvany et al. (2012).

4.3.2. Volcano slope and elevation

The morphology of volcanic structure depends on the type of magma emitted, the eruption dynamics, and also on deformation and differential growth processes (e.g., Rowland and Garbeil, 2000; Michon and Saint Ange, 2008; Grosse et al., 2009). The flanks of stratocones, which produce silicic magmas, generally present an expo nential slope reaching values of around 30° close to the edifice summit (Grosse et al., 2014; Favalli et al., 2014). In contrast, shield volcanoes, which emit basalts, are classically characterized by gentle flanks with slopes ranging between 5 and 10° (e.g. Mark and Moore, 1987; Hürlimann et al., 2004; Grosse et al., 2014), and soft slopes toward the summit (Grosse and Kervyn, 2018). Nonetheless, these volcanoes can also present steeper flanks (around 20°) in areas of cone concentration (Rowland and Garbeil, 2000) or flank deformation (Michon and Saint Ange, 2008; Cayol et al., 2014).

During the evolution of Piton des Neiges, the magma composition evolved from basaltic (La Montagne to PN2), to moderately differenti ated (PN3) and then to silicic magmas (PN4; Kluska, 1997). The DCE di agrams for PN (Fig. 9a; Fig. S4) show that the intermediate part of the flanks of PN1, PN2 and PN3 were characterized by similar slopes (aver age of ~9 10° above 500 m asl), and that at low elevation, the slopes of PN2 and PN3 seems to soften (around 7°). These slope values and their decrease at low elevation are typical of basaltic volcanoes worldwide (Grosse and Kervyn, 2018). Moreover, these similar slope values be tween PN2 and PN3 suggest that the magma composition change de scribed between these stages (Upton and Wadsworth, 1966) did not influence the geometry of the flanks of PN3. Conversely, PN4 shows a different geometry than the previous edifices. It presents an exponential increase in slope from ~5° (750 1600 m asl) to more than 14° toward the top (1600 3000 m asl, Fig. S4; Gayer et al., 2019). These low slopes at low elevation can be explained by the accumulation of lava flows, confined in erosional depressions such as the Marsouins and Salazie paleo cirques (Gayer et al., 2019). In contrast, the abundance of pyro clastic deposit in the scarp of Rond de Bras Rouge (Fig. S5) suggests that the steep slopes toward the summit result from the building of a pyroclastic rich summit, partially covered by the viscous lava flows. Thus, the high altitude reached by PN4, despite a short period of activity, can be explained by the effect of great vertical growth due to a magma explosivity higher than with basalts, leading to pyroclastic accumula tions in the summit area.

For the Piton de la Fournaise, our characteristics reconstructions of PF1 and PF3 reveal contrasting flank morphologies with a fairly constant slope of ~8 9° for PF1 below 1500 m asl and for PF3, an average slope of ~14° below 1500 m asl, which then flattens out above 2000 m asl (Fig. 9b; Fig. S4). The steep average slope of PF3, unusual for a basaltic volcano, results from the presence of two areas of steep slopes (between 20 and 30°) on its south and north flanks (which merge on the eastern flank; Rowland and Garbeil, 2000; Michon and Saint Ange,

2008). These slopes are interpreted as the result of gravitational defor mations that can promote potential edifices instabilities, either above a weak hydrothermal system (Michon and Saint Ange, 2008) or by mass displacement related to successive intrusions (Peltier et al., 2015). Such instability has been evidenced for Piton de la Fournaise by the vast de bris avalanche deposits that cover its eastern submarine flanks (Lénat et al., 1989; Oehler et al., 2008; Le Friant et al., 2011) and we anticipate that the growth of Piton de la Fournaise on the flank of Piton des Neiges (and perhaps over the dismantled Alizés volcano) is disturbed and lim ited by its abutment to the Piton des Neiges.

While the overall geometry of PN4 can be deduced thanks to the presence of control points close to the center of the edifice, the ge ometry of the top zone of PN1, PN2 and PN3 is far less well constrained. Salvany et al. (2012) proposed extrapolating the sum mit part of PN3 with a third degree polynomial, which gives a sum mit elevation of ~3700 m. Yet, the distribution of the control points of PN3 on the DCE diagram does not support such a polynomial extrap olation since there is a constant mean slope (with both *LR* and *SP* methods) between 1000 m asl and the highest control point at 2900 m asl, located at 5 km from the inferred volcanic center (Fig. 9a; Fig. S4). In addition, given the diversity of summit morphologies and the possibility of summit calderas (see Grosse et al., 2014 for a compilation of the summit morphologies of shield volcanoes and stratocones), we consider it too speculative to estimate the altitudes of the summits at the different stages of growth of Piton des Neiges and Piton de la Fournaise. Nevertheless, the profiles of the different PF and PN in the DCE diagrams suggest that the successive edifices of Piton de la Fournaise were systematically smaller than those of Piton des Neiges (Fig. 9).

Finally, we can deduce the degrees of ellipticity and symmetry of the studied volcanoes. These parameters can be inferred from the distribution of the control points on the DCE diagrams. As explained in Section 2.1, narrow trends drawn by the control points result from symmetric and circular volcanoes like Mayon, Licancabur and Fuji volcanoes (Figs. 3, 10; Fig. S1), whereas asymmetric and/or elliptic volcanoes produce a scattered distribution of the control points (e.g. Mt. Cameroon, Ambae and the volcanoes of Hawaii) (Figs. 3, 10; Fig. S2). The reconstructions of the characteristics of the succes sive edifices of Piton des Neiges and Piton de la Fournaise, are constrained by control points located at more than 180° around the eruptive centers (i.e. half of an edifice), so we deduce that PN1, PN2 and PN3 were nearly circular and symmetric (i.e. narrow distri bution of the control points) while the scattering of control points for PF3 suggests it was irregular in shape (Fig. 9). We interpret the irreg ularity of PF3 as mainly due to the NE and SE rift zones of Piton de la Fournaise along which the recurrent effusion of lava flows progres sively built two smoothed radial ridges (Fig. 5a). Conversely, the symmetry and near circularity of PN1, PN2 and PN3 suggest that the volcanic activity along the Etang Salé and N120 rift zones was low enough not to build elongated reliefs and, therefore, that the building of these edifices primarily results from a central activity ().

4.3.3. Hypothesis on rates of construction of Piton des Neiges

Based on the superposition of the profiles of the intermediate parts of PN1, PN2 and PN3, in the DCE diagram (Fig. 9a), our results suggest that the successive edifices were similar in size. Nevertheless, the size and slopes of an effusive volcanic cone depends on the duration of the magmatic activity, the altitude of the pre existing topography on which the edifice grew (even if it is irregular, such as valleys and planezes), the viscosity of the magma involved in the construction pe riod, and the rate of magma emission. While landform reconstruction techniques have been used to estimate the volumes of magma emitted by volcanoes at different stages of their history (e.g. Lahitte et al., 2012; Germa et al., 2015), accurate estimates are rarely possible. Indeed, both the surface topography prior to construction and the paleo erosion rates are often unknown and must therefore be assumed. However, in the case of successive periods of construction and dismantling resulting in successive edifices of similar size, the volume dismantled is compen sated for by the volume subsequently emitted, as follows:

$$Tc_n \times Dc_n \quad Td_{n\ 1} \times Dd_{n\ 1} \tag{3}$$

where *Tc*, *Td* and *Dc*, *Dd* are the rates of construction and dismantling and the durations of construction and dismantling, respectively, and *n* the stage in the history of the edifice. In this case, the relative im portance of the construction rates can be derived using construction and dismantling times, and hypothesis on only the dismantling rates. Fig. 11, which is based on the published radiometric ages (see for the synthesis Salvany et al., 2012), shows the duration of the construc tion and dismantling periods of Piton des Neiges. These durations are progressively shorter from PN1 to PN4 and the decrease in time is more important for the dismantling periods than for the construc tion periods. As a consequence, the activity of PN1 was shorter than the previous dismantling period, whereas the building of PN3 was significantly longer than its previous dismantling period. In order to accurately estimate the construction rates for the different stages of Piton des Neiges, dismantling rates are needed. As previously mentioned, paleo dismantling rates are nearly impossible to esti mate and, more generally, the evolution of overall erosion rates dur ing the Late Cenozoic is a matter of debate (Willenbring and von Blanckenburg, 2010; Herman et al., 2013; Schildgen et al., 2018). Nevertheless, one could follow the hypothesis of a constant erosion rate over the last 2 Myrs (Willenbring and von Blanckenburg, 2010; Karátson et al., 2016) and assume a constant dismantling rate for Ré union since increases in erosion rates linked to climatic variations have mainly affected mountainous areas where glaciations have fa vored erosion (by glaciers; Herman et al., 2013). Assuming a con stant dismantling rate *Td* for PN1, PN2 and PN3 (which may not accurately account for flank collapses), and using their respective durations of construction *Dc* and dismantling *Dd*, we suspect that the construction rate of PN2 was lower than that of PN1 by 20%, and most importantly, that the construction rate drastically de creased between PN2 and PN3 to reach only 23% of the construction rate of PN1 (Fig. 11). This suggests an overall decrease in the magma input rate during the history of Piton des Neiges, which is in agree ment with observations of the petrological evolution of the magma (Valer et al., 2017) and which is here quantified from a simple mor phological approach. Finally, it is worth noting that this drop of magma input rate coincides with a change of magma composition of Piton de la Fournaise from slightly differentiated alkaline magmas to basalts of the transitional series (Albarède et al., 1997).

5. Conclusions

In this study, we present a simple geometrical approach to find both the location of the long term eruption center and the general shape of a volcano from portions of the remnant surface. This method successfully reveals the center of eruption for a wide range of volcanoes geometries, from circular to elliptic and even for asymmetrical shapes. Like other methods, our approach is sensitive to the regularity of the volcano but can be used to characterize potential asymmetry.

This simple geometrical approach suggests that the location of the volcanic center of Piton des Neiges has been stable for the last 1.4 Myr while the center of Piton de la Fournaise has been migrating eastward for the last ~300 kyr, in support of previous interpretation based on other types of geological and geophysical data. Our results further sug gest that Piton des Neiges is the dominant volcano in the building of the island and that Piton de la Fournaise appears to be a smaller edifice growing on its edge. Despite evidences for the contribution of two other volcanoes in the construction of Réunion, it appears the Piton des Neiges is now the main structure of the whole island of Réunion. Finally, from our reconstitutions of the different stages of the Piton des Neiges, we

have modeled the relative importance of its magmatic activity, and we suggest an increasing deceleration of its magma input rates since 2Myrs.

This broad analysis of volcanoes around the world, and detailed analysis of Réunion, suggests our simple method is a useful alternative in the absence of more detailed instrumentation and analysis.

Declaration of competing interest

The authors declare that they have no known competing financial interests or personal relationships.

that could have appeared to influence the work reported in this paper.

Acknowledgements

This work was supported by funding from INTRACRUE program (Office de l'EAU, Univeristé de La Réunion, Université de Bretagne Occidentale). We thank P. Lopez, and O. Deveauchelle for discussions, and the reviewers D. Karàtson, P.A. Kervyn and S. Camiz for helping improving the manuscript.

Data availability

A python version of the function is available on Github https://github.com/egayer/ConeCone.

Appendix A. Supplementary data

Supplementary data to this article can be found online at https://doi.org/10.1016/j.geomorph.2021.107900.

References

Albarède, F., Luais, B., Fitton, G., Semet, M., Kaminski, E., Upton, B.G.J., Bachèlery, P., Cheminée, J.-L., 1997. The geochemical regimes of Piton de la Fournaise Volcano (Réunion) during the last 530 000 years. J. Petrol. 38, 171–201.

Albert, S., Flores, O., Michon, L., Strasberg, D., 2020. Dating young (<1000 yr) lava flow eruptions of Piton de la Fournaise volcano from size distribution of long-lived pioneer trees. J. Volcanol. Geotherm. Res. 401, 106974.

Allemand, P., Delacourt, C., Lajeunesse, E., Devauchelle, O., Beauducel, F., 2014. Erosive effects of the storm Helena (1963) on Basse Terre Island (Guadeloupe — Lesser Antilles Arc). Geomorphology 206, 79–86.

Babonneau, N., Delacourt, C., Cancouët, R., Sisavath, E., Bachèlery, P., Mazuel, A., Jorry, S.J., Deschamps, A., Ammann, J., Villeneuve, N., 2013. Direct sediment transfer from land to deep-sea: Insights into shallow multibeam bathymetry at La Réunion Island. Mar. Geol. 346, 47–57.

Bachèlery, P., Mairine, P., 1990. Evolution volcano-structurale du Piton de la Fournaise depuis 0,53 Ma. In: Lénat, J.F. (Ed.), Le Volcanisme de la Réunion - Monographie. Centre de Recherches Volcanologiques, pp. 213–242.

Bachèlery, P., Robineau, B., Courteaud, M., Savin, C., 2003. Avalanches de débris sur le flanc occidental du volcan-bouclier Piton des Neiges (Reunion). Bulletin de la Société Géologique, France. vol. 174, pp. 125–140.

Bachèlery, P., Mairine, P., Odon, O., Billard, G., Nehlig, P., Quinquis, J.P., Bucelle, M., 2006. Carte Geologique de la Réunion à 1/100 000 (Edition BRGM).

Carracedo, J.C., 1994. The Canary Islands: an example of structural control on the growth of large oceanic-island volcanoes. J. Volcanol. Geotherm. Res. 60, 225–241.

Cayol, V., Catry, T., Michon, L., Chaput, M., Famin, V., Bodart, O., Froger, J.L., Romagnoli, C., 2014. Sheared sheet intrusions as mechanism for lateral flank displacement on basaltic volcanoes: applications to Réunion Island volcanoes. J. Geophys. Res. Solid Earth 119, 7607–7635.

Chaput, M., Famin, V., Michon, L., 2017. Sheet intrusions and deformation of Piton des Neiges, and their implication for the volcano-tectonics of La Réunion. Tectonophysics 717, 531–546.

Chevallier, L., Vatin-Perignon, N., 1982. Volcano-structural evolution of Piton des Neiges, Reunion Island, Indian Ocean. Bull. Volcanol. 45, 285–298.

Cioni, R., Santacroce, R., Sbrana, A., 1999. Pyroclastic deposits as a guide for reconstructing the multi-stage evolution of the Somma-Vesuvius Caldera. Bull. Volcanol. 61 (4), 207–222.

de Voogd, B., Palomé, S.P., Hirn, A., Charvis, P., Gallart, J., Rousset, D., Dañobeitia, J., Perroud, H., 1999. Vertical movements and material transport during hotspot activity: Seismic reflection profiling offshore La Réunion. J. Geophys. Res. Solid Earth 104, 2855–2874.

Dibacto, S., Lahitte, P., Karátson, D., Hencz, M., Szakács, A., Biró, T., Kovács, I., Veres, D., 2020. Growth and erosion rates of the East Carpathians volcanoes constrained by numerical models: tectonic and climatic implications. Geomorphology 368, 107352.

Dieterich, J.H., 1988. Growth and persistence of Hawaiian Volcanic rift zones. J. Geophys. Res. 93, 4258–4270.

Duffield, W.A., Stieltjes, L., Varet, J., 1982. Huge landslide blocks in the growth of piton de la fournaise, La réunion, and Kilauea volcano, Hawaii. J. Volcanol. Geotherm. Res. 12, 147–160.

Duncan, R.A., 1990. The volcanic record of the Réunion hotspot. Proceedings of the Ocean Drilling Program, Scientific Results. vol. 115, pp. 3–10.

Favalli, M., Karátson, D., Yepes, J., Nannipieri, L., 2014. Surface fitting in geomorphology - examples for regular-shaped volcanic landforms. Geomorphology 221, 139–149.

Ferrier, K.L., Huppert, K.L., Perron, J.T., 2013a. Climatic control of bedrock river incision. Nature 496, 206–209.

Ferrier, K.L., Perron, J.T., Mukhopadhyay, S., Rosener, M., Stock, J.D., Huppert, K.L., Slosberg, M., 2013b. Covariation of climate and long-term erosion rates across a steep rainfall gradient on the Hawaiian island of Kaua'i. Geol. Soc. Am. Bull. 125, 1146–1163.

Francis, P.W., Abbot, B.M., 1973. Sizes of conical volcanoes. Nature 244, 22–23.

Gailler, L.S., Lénat, J.F., 2010. Three-dimensional structure of the submarine flanks of La Réunion inferred from geophysical data. J. Geophys. Res. Solid Earth 115, B12105.

Garcin, M., Poisson, B., Pouget, R., 2005. High rates of geomorphological processes in a tropical area: the Remparts River case study (Réunion Island, Indian Ocean). Geomorphology 67, 335–350.

Gayer, E., Lopez, P., Michon, L., 2014. DEM-based model for reconstructing volcano's morphology from primary volcanic landforms. Geophysical Research Abstracts 16, EGU2014-10701, Vienna, Austria.

Gayer, E., Michon, L., Louvat, P., Gaillardet, J., 2019. Storm-induced precipitation variability control of long-term erosion. Earth Planet. Sci. Lett. 517, 61–70.

Germa, A., Lahitte, P., Quidelleur, X., 2015. Construction and destruction of Mont Pelée volcano: volumes and rates constrained from a geomorphological model of evolution. J. Geophys. Res. Earth Surf. 120, 1206–1226.

Gillot, P., Lefevre, J., Nativel, P., 1994. Model for the structural evolution of the volcanos of Reunion island. Earth Planet. Sci. Lett. 122, 291–302.

Grosse, P., Kervyn, M., 2018. Morphometry of terrestrial shield volcanoes. Geomorphology 304, 1–14.

Grosse, P., van Wyk de Vries, B., Petrinovic, I.A., Euillades, P.A., Alvarado, G.E., 2009. Morphometry and evolution of arc volcanoes. Geology 37, 651–654.

Grosse, P., van Wyk de Vries, B., Euillades, P.A., Kervyn, M., Petrinovic, I.A., 2012. Systematic morphometric characterization of volcanic edifices using digital elevation models. Geomorphology 136, 114–131.

Grosse, P., Euillades, P.A., Euillades, L.D., Wyk de Vries, B., 2014. A global database of composite volcano morphometry. Bull. Volcanol. 76, 784.

Herman, F., Seward, D., Valla, P.G., Carter, A., Kohn, B., Willett, S.D., Ehlers, T.A., 2013. Worldwide acceleration of mountain erosion under a cooling climate. Nature 504, 423–426.

Hildenbrand, A., Gillot, P.-Y., le Roy, I., 2004. Volcano-tectonic and geochemical evolution of an oceanic intra-plate volcano: Tahiti-Nui (French Polynesia). Earth Planet. Sci. Lett. 217, 349–365.

Hildenbrand, A., Gillot, P.-Y., Marlin, C., 2008. Geomorphological study of long-term erosion on a tropical volcanic ocean island: Tahiti-Nui (French Polynesia). Geomorphology 93, 460–481.

Hürlimann, M., Martí, J., Ledesma, A., 2004. Morphological and geological aspects related to large slope failures on oceanic islands. Geomorphology 62, 143–158.

Karátson, D., Favalli, M., Tarquini, S., Fornaciai, A., Wörner, G., 2010. The regular shape of stratovolcanoes: a DEM-based morphometrical approach. J. Volcanol. Geotherm. Res. 193, 171–181.

Karátson, D., Telbisz, T., Wörner, G., 2012. Erosion rates and erosion patterns of Neogene to Quaternary stratovolcanoes in the Western Cordillera of the Central Andes: an SRTM DEM based analysis. Geomorphology 139–140, 122–135.

Karátson, D., Yepes, J., Favalli, M., Rodríguez-Peces, M.J., Fornaciai, A., 2016. Reconstructing eroded paleovolcanoes on Gran Canaria, Canary Islands, using advanced geomorphometry. Geomorphology 253, 123–134.

Kluska, J., 1997. Evolution magmatique et morphostructurale du Piton des Neiges au cours des derniers 500 000 ans. (Unpublished PhD thesis). Université Paris Sud, p. 93.

Kreemer, C., 2009. Absolute plate motions constrained by shear wave splitting orientations with implications for hot spot motions and mantle flow. J. Geophys. Res. Solid Earth 114.

Labazuy, P., 1996. Recurrent landslides events on the submarine flank of Piton de la Fournaise volcano (Reunion Island). Geol. Soc. Spec. Publ. 110, 295–306.

Lacey, A., Ockendon, J.R., Turcotte, D.L., 1981. On the geometrical form of volcanoes. Earth Planet. Sci. Lett. 54, 139–143.

Lahitte, P., Samper, A., Quidelleur, X., 2012. DEM-based reconstruction of southern Basse-Terre volcanoes (Guadeloupe archipelago, FWI): contribution to the Lesser Antilles Arc construction rates and magma production. Geomorphology 136, 148–164.

Lamb, M.P., Howard, A.D., Dietrich, W.E., Perron, J.T., 2007. Formation of amphitheater-headed valleys by waterfall erosion after large-scale slumping on Hawai'i. Geol. Soc. Am. Bull. 119 (7–8), 805–822.

Le Friant, A., Lebas, E., Clément, V., Boudon, G., Deplus, C., de Voogd, B., Bachèlery, P., 2011. A new model for the evolution of la Réunion volcanic complex from complete marine geophysical surveys. Geophys. Res. Lett. 38 (n/a-n/a).

Lebas, E., le Friant, A., Deplus, C., de Voogd, B., 2018. Understanding the evolution of an oceanic intraplate volcano from seismic reflection data: a new model for La Réunion, Indian Ocean. J. Geophys. Res. Solid Earth 123, 1035–1059.

Lénat, J.F., Vincent, P., Bachèlery, P., 1989. The off-shore continuation of an active basaltic volcano: Piton de la Fournaise (Réunion Island, Indian Ocean); structural and geomorphological interpretation from sea beam mapping. J. Volcanol. Geotherm. Res. 36.

Lénat, J.-F., Gibert-Malengreau, B., Galdéano, A., 2001. A new model for the evolution of the volcanic island of Réunion (Indian Ocean). J. Geophys. Res. Solid Earth 106, 8645–8663.

Lerebour, P., 1987. Etude du forage du Grand Brûlé (Piton de la Fournaise, île de la Réunion): lithostratigraphie, pétrologie, minéralogies primaire et secondaire. Conséquences sur l'évolution volcanostructurale du massif du Piton de la Fournaise. (Unpublished PhD thesis). Université Paris Sud, p. 198.
Letourneur, L., Peltier, A., Staudacher, T., Gudmundsson, A., 2008. The effects of rock heterogeneities on dyke paths and asymmetric ground deformation: the example of Piton de la Fournaise (Réunion Island). J. Volcanol. Geotherm. Res. 173, 289–302.
Mairine, P., Bachèlery, P., 1997. Major erosional period in the building of Piton de la Fournaise (Reunion island). C. R. Acad. Sci. 325, 243–249.
Malengreau, B., Lénat, J.F., Froger, J.L., 1999. Structure of Reunion Island (Indian Ocean) inferred from the interpretation of gravity anomalies. J. Volcanol. Geotherm. Res. 88, 131–146.
Mark, R., Moore, J., 1987. Slopes of the Hawaiian ridge. US Geol. Surv. Prof. Pap. 1350, 101–107.
Mazuel, A., Sisavath, E., Babonneau, N., Jorry, S.J., Bachèlery, P., Delacourt, C., 2016. Turbidity current activity along the flanks of a volcanic edifice: the Mafate volcaniclastic complex, La Réunion Island, Indian Ocean. Sediment. Geol. 335, 34–50.
McDougall, I., 1971. The geochronology and evolution of the young volcanic island of Réunion, Indian Ocean. Geochim. Cosmochim. Acta 35, 261–288.
Merle, O., Lénat, J.-F., 2003. Hybrid collapse mechanism at Piton de la Fournaise volcano, Reunion Island, Indian Ocean. J. Geophys. Res. Solid Earth 108 (B3), 2166.
Merle, O., Mairine, P., Michon, L., Bachèlery, P., Smietana, M., 2010. Calderas, landslides and paleo-canyons on Piton de la Fournaise volcano (La Réunion Island, Indian Ocean). J. Volcanol. Geotherm. Res. 189, 131–142.
Michon, L., Saint-Ange, F., 2008. Morphology of Piton de la Fournaise basaltic shield volcano (La Réunion Island): characterization and implication in the volcano evolution. J. Geophys. Res. Solid Earth 113, B03203.
Michon, L., Lénat, J.-F., Bachèlery, P., di Muro, A., 2016. Geology and Morphostructural Evolution of Piton de la Fournaise. Active Volcanoes of the Southwest Indian Ocean. Springer Berlin Heidelberg, Berlin, Heidelberg, pp. 45–59.
Muller, R.D., Royer, J.Y., Lawyer, L.A., 1994. Revised plate motions relative to the hotspots from combined Atlantic and indian-ocean hotspot tracks - reply. Geology 22, 277–278.
Murphy, B.P., Johnson, J.P.L., Gasparini, N.M., Sklar, L.S., 2016. Chemical weathering as a mechanism for the climatic control of bedrock river incision. Nature 532, 223–227.
Naumann, T., Geist, D., 2000. Physical volcanology and structural development of Cerro Azul Volcano, Isabela Island, Galapagos: implications for the development of Galapagos-type shield volcanoes. Bull. Volcanol. 61, 497–514.
Oehler, J.-F., Lénat, J.-F., Labazuy, P., 2008. Growth and collapse of the Reunion Island volcanoes. Bull. Volcanol. 70, 717–742.
Ollier, C., 1988. Volcanoes. Blackwell, Oxford (228 pp.).
Peltier, A., Got, J.-L., Villeneuve, N., Boissier, P., Staudacher, T., Ferrazzini, V., Walpersdorf, A., 2015. Long-term mass transfer at Piton de la Fournaise volcano evidenced by strain distribution derived from GNSS network. J. Geophys. Res. Solid Earth 120, 1874–1889.
Peterson, D.W., Moore, R.B., 1987. Geologic history and evolution of geologic concepts, Island of Hawaii. Volcanism in Hawaii. vol. 1350, pp. 149–189.
Quidelleur, X., Holt, J.W., Salvany, T., Bouquerel, H., 2010. New K-Ar ages from La Montagne massif, Réunion Island (Indian Ocean), supporting two geomagnetic events in the time period 2.2–2.0 Ma. Geophys. J. Int. 182, 699–710.
Rançon, J.P., Lerebour, P., Augé, T., 1989. The Grand Brule exploration drilling: new data on the deep framework of the Piton de la Fournaise volcano. Part 1: lithostratigraphic units and volcanostructural implications. J. Volcanol. Geotherm. Res. 36, 113–127.
Rousset, D., Lesquer, A., Bonneville, A., Lénat, J.F., 1989. Complete gravity study of Piton de la Fournaise volcano, Reunion Island. J. Volcanol. Geotherm. Res. 36, 37–52.
Rowland, S.K., 1996. Slopes, lava flow volumes, and vent distributions on Volcán Fernandina, Galápagos Islands. J. Geophys. Res. Solid Earth 101, 27657–27672.
Rowland, S.K., Garbeil, H., 2000. Slopes of oceanic basalt volcanoes. In: Mouginis-Mark, P. J., Crisp, J.A., Fink, J.H. (Eds.), Remote Sensing of Active Volcanoes. Geophysical Monograph Series vol. 113, pp. 223–247.
Saint-Ange, F., Savoye, B., Michon, L., Bachèlery, P., Deplus, C., de Voogd, B., Dyment, J., le Drezen, E., Voisset, M., le Friant, A., Boudon, G., 2011. A volcaniclastic deep-sea fan off La Reunion Island (Indian Ocean): gradualism versus catastrophism. Geology 39, 271–274.
Saint-Ange, F., Bachèlery, P., Babonneau, N., Michon, L., Jorry, S.J., 2013. Volcaniclastic sedimentation on the submarine slopes of a basaltic hotspot volcano: Piton de la fournaise volcano (la réunion island, indian ocean). Mar. Geol. 337, 35–52.
Salvany, T., Lahitte, P., Nativel, P., Gillot, P.-Y., 2012. Geomorphic evolution of the Piton des Neiges volcano (Réunion Island, Indian Ocean): competition between volcanic construction and erosion since 1.4 Ma. Geomorphology 136, 132–147.
Schildgen, T.F., Beek, P.A., Sinclair, H.D., Thiede, R.C., 2018. Spatial correlation bias in late-Cenozoic erosion histories derived from thermochronology. Nature 1–16.
Smietana, M., 2011. Pétrologie, géochronologie (K-Ar) et géochimie élémentaire et isotopique (Sr, Nd, Hf, Pb) de laves anciennes de La Réunion: Implications sur la Construction de l'édifice volcanique. (Unpublished PhD thesis). Université de La Réunion, p. 364.
Smietana, M., Bachèlery, P., Hémond, C., 2010. Heterogeneity in the mantle source of La Reunion Island. Geochim. Cosmochim. Acta 74 (A-972).
Székely, B., Karátson, D., 2004. DEM-based morphometry as a tool for reconstructing primary volcanic landforms: examples from the Börzsöny Mountains, Hungary. Geomorphology 63, 25–37.
Terry, J.P., Garimella, S., Kostaschuk, R.A., 2002. Rates of floodplain accretion in a tropical island river system impacted by cyclones and large floods. Geomorphology 42, 171–182.
Thouret, J.C., 1999. Volcanic geomorphology-an overview. Earth-Sci. Rev. 47, 95–131.
Upton, B.G.J., Wadsworth, W.J., 1966. The basalts of Réunion Island, Indian Ocean. Bull. Volcanol. 29, 7–23.
Valer, M., Bachèlery, P., Schiano, P., 2017. The Petrogenesis of Plagioclase-ultraphyric Basalts from La Réunion Island. J. Petrol. 58, 675–698.
Well, A.D., Myers, J.L., 2002. Research Design & Statistical Analysis. Taylor & Francis, Oxford.
Willenbring, J.K., von Blanckenburg, F., 2010. Long-term stability of global erosion rates and weathering during late-Cenozoic cooling. Nature 1–4.